CHAPTER 5

Volcanic clouds

Fred Prata, Kenneson Dean, Matthew Watson

5.1 OVERVIEW

Volcanism has been an unrivaled contributor of material to the atmosphere over the course of Earth history. Emissions from volcanoes can include gases, liquid droplets, and solid particles across a wide range of chemical variation. The primary products from active volcanism are water (in three phases), carbon dioxide, and lithic fragments derived from upwelling magma and country rock. Other gases include SO_2 (see Chapter 6), HF, HCl, HBr, H_2S, H_2O, and a host of trace gases. The mineral-based part of the plume is typically known by the catch-all term "volcanic ash". These constituents are injected, often at very high velocity, into the atmosphere and regularly reach several kilometers in altitude. Emissions from volcanism can have dimensions of hundreds of kilometers and have been observed to circumnavigate the globe (e.g., Bluth *et al.*, 1992). Volcanic emissions typically begin as a complex, multiphase, coherent outburst from a point source (or occasionally a linear feature such as a fissure). Ash in volcanic emissions is sourced from magmatic fragmentation and subsumation of country rock. This transmits information on eruptive conditions and processes from the subsurface to the atmosphere and, eventually, forms a deposit as the ash settles out of the atmosphere. Observations of both volcanic ash in situ in the atmosphere and the subsequent deposits have been used for over three decades to infer erupted mass, eruption rate, column height, and duration of the eruption (e.g., Walker, 1971; Pyle, 1989; Wen and Rose, 1994). Fragmentation front propagation in the conduit is at the forefront of current research into explosive volcanism (e.g., Kennedy *et al.*, 2005; Zobin and Jiménez, 2008). This imparts control over the particle size distribution of ash which can be inverted from observation, again to constrain subsurface processes.

Volcanic emissions from explosive activity are on a scale, and present hazards, that are best observed from the synoptic perspective afforded by satellite sensors. The literature is replete with examples of observation of volcanic ash in the atmosphere from satellite-borne sensors dating back 25 years (e.g., Prata, 1989a, b; Wen and Rose, 1994; Schneider *et al.*, 1999; Prata and Grant, 2001; Watson *et al.*, 2004). There are several ways to describe the style of volcanic emission; these are used interchangeably in the literature and, hence, it is worth carefully reiterating the conventional definitions.

5.2 DEFINITIONS

Volcanic cloud: airborne component of an explosive eruption and a term used to mean volcanic emissions during any type of eruption. Usually, though not always, associated with an emission that has detached from the vent.

Eruption cloud: volcanic cloud not attached to the volcano typically associated with explosive activity.

K.G. Dean and J. Dehn (eds.), *Monitoring Volcanoes in the North Pacific*,
Springer Praxis Books, DOI 10.1007/978-3-540-68750-4_5

Ash or SO_2 cloud: component-specific description of volcanic emission. Something of a misnomer that encourages the community to consider emissions to be heavily dominated by a single species.

Drifting ash cloud: more complete description of emission, indicating explicitly that the cloud no longer feels any contribution from the vent.

Volcanic plume: Volcanic emission still attached to the volcano.

Whilst these descriptions appear somewhat pedantic, the issue of whether or not the emission is still being contributed to is of vital importance. For example, arguably the most important parameter retrieved by satellite is total ash mass, as it scales to eruption rate and, hence, the size of the eruption. The calculation of any mass-based parameter is significantly different in the two scenarios. A drifting cloud's mass is, by definition, independent of ongoing activity and can be observed to decrease over time as the ash falls out. Ash cloud masses (typically reported in kilotonnes) are thus derived by summing the mass of individual pixels (techniques to retrieve ash mass are discussed in Section 5.10). Conversely, a plume's mass is not a very helpful number, as the plume is continually being contributed to by the volcanic vent. Instead, an emission rate, with units of mass per unit time (typically reported in tonnes per day), is derived by slicing through the plume, integrating the transect's mass and multiplying by the plume speed.

Drifting ash clouds represent a significant hazard to aviation and can have detectable concentrations thousands of kilometers from the source. There are several well-known examples of aircraft–ash interaction, notably Galunggung (Indonesia) in 1982 (BA Flight 9) and Redoubt (Alaska) in 1989 (KLM Flight 867) (see DVD for a description of these events). In both examples a large jet airliner suffered a four-engine failure before managing to restart the engines and prevent catastrophe. Plumes, whilst still dangerous, represent a more limited threat to aircraft as they are constrained spatially to be close to the vent. However, they can still represent a significant issue for airports such as Catania (Sicily) and Kona/Hilo (Hawaii) (Figure 5.1). The airport at Anchorage is regularly affected by emissions from volcanoes in the region, depending on wind conditions. However, the most significant risk in the NOPAC region remains between aircraft at cruising altitude with drifting ash clouds from remote vents.

5.3 STRUCTURE OF VOLCANIC PLUMES AND CLOUDS

5.3.1 Plume fluid dynamics

Many excellent images of volcanic plumes have been captured over the last decades. Volcanic centers are the target of routine observations from Earth observation (EO) sensors (including ASTER and MODIS—see the prelims for a list of acronyms) causing plumes to be more regularly captured than drifting clouds. This is compounded, of course, by the fact that plumes are also much more common. This chapter is not the place to undertake a rigorous description of the fluid dynamical phenomena observed in volcanic plumes simply to pique the reader's interest. For example, the image in Figure 5.1a shows ladder-like structures that may be related to the Brunt–Väisälä frequency and image 5.1b shows the interaction of the plume with an atmospheric eddy caused by the

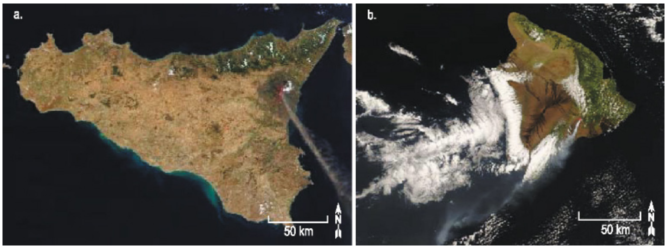

Figure 5.1. Natural-color MODIS satellite images of plumes from Mt. Etna, Sicily, July 22, 2001 (a) and Kīlauea, Hawaii, August 7, 2008 (b) disrupting air traffic at airports in Catania and Kona, respectively (images are courtesy of NASA Earth Observatory website).

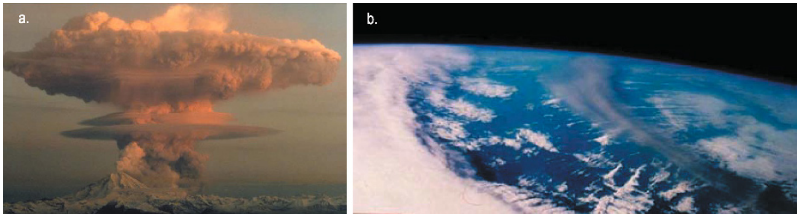

Figure 5.2. Photographs of a proximal cloud (a) of Redoubt Volcano, April 21, 1990 (courtesy of R. Clucas) and distal cloud (b) from Spurr Volcano, September 9, 1992, from the NASA Space Shuttle.

complex topography of the Big Island of Hawaii. Here the particles released from the vent are able to act as cloud condensation nuclei in the warm, tropical atmosphere.

5.3.2 Drifting ash clouds

Drifting ash clouds present a range of morphologies depending on atmospheric conditions (including wind strength and temperature structure), eruption source strength, and, critically, elapsed time since eruption. Figure 5.2 shows two classic examples, Mt. Redoubt shortly after eruption (a) showing a broadly circular shape (when viewed from above) and Mt. Spurr (b), where the cloud became very elongate as it drifted over the conterminous United States. As a general rule, the aspect ratio (and complexity) of the cloud shape increases over time (see Mt. Spurr example, Figure 5.3).

5.4 COMPOSITION, SIZE, AND SHAPE

Volcanic ash is an unconsolidated mixture of sand to dust-sized (1 to 0.001 mm) rock and mineral fragments produced during explosive eruptions. Rock fragments are typically glassy and form as liquid magma quenches following its eruption at the Earth's surface. Mineral fragments found within the glass include plagioclase feldspar, horn-

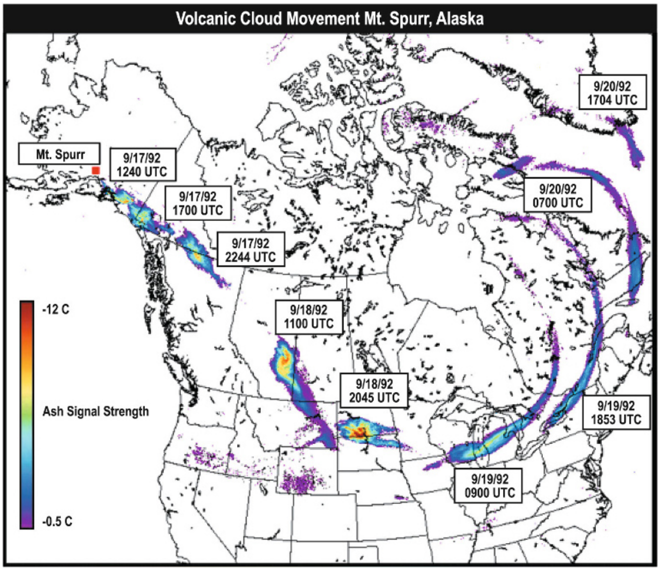

Figure 5.3. Increase in cloud aspect ratio over time as it drifts across North America. This example is from the September 1992 eruption of Mt. Spurr and is based on AVHRR brightness temperature differences—dates and times of the AVHRR images are shown in the boxes (courtesy of Dave Schneider, USGS).

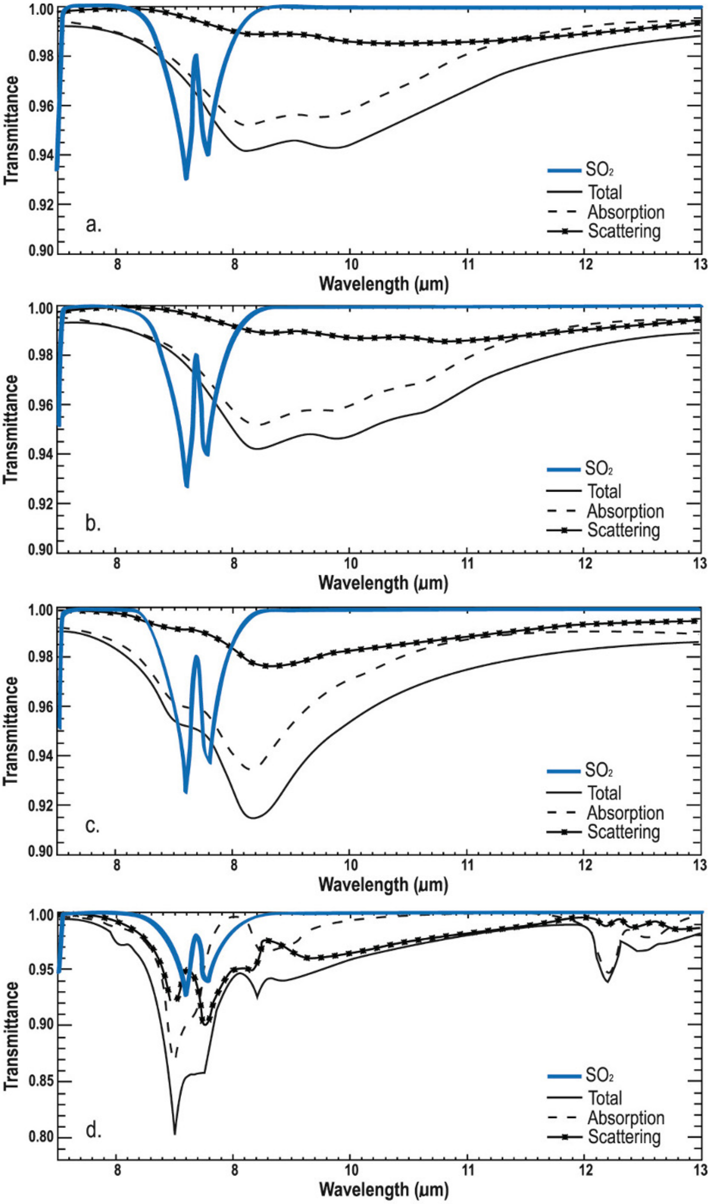

Figure 5.4. Total, scattering, and absorption transmissions for (a) basalt, (b) andesite, (c) rhyolite, and (d) quartz as a function of wavelength. The measurements are based on 10^5 particles per m^2, a log-normal distribution with a variance of 0.74, and an effective radius of 0.5 for 7.5–13 µm. The transmittance of SO_2 is overlaid in blue. The transmittance scale in (d) is slightly longer than in (a), (b), and (c).

blende, and pyroxene. The minerals are based upon combinations of Fe, Al, K, Na, and other metals in combination with silicate groups. Mineralization, where preserved, is the pressure/temperature history of the melt on its ascent to the surface. The amount of silica in the ash is a ramification of the magma's parent composition. This has a significant effect on the ash's radiative properties (see Figure 5.4) and our ability to distinguish it from other species (see Kearney, 2010).

The size of volcanic ash particles is an important parameter, controlling physical behavior, direct impact on humans, and the effects the ash exerts on the Earth's radiation budget (ERB). Volcanic ash is typically described in terms of the particle size distribution rather than by a single size (e.g., radius). The distributions typically have a mathematical form and are constrained by two to three additional parameters. In most cases the form is of a well-known mathematical type, log-normal (ZOLD) is often used, and the parameters completely describe the distribution (in the case of the log-normal distribution the variance and mean are sufficient).

5.5 EVOLUTION OF A VOLCANIC CLOUD

The evolution of a volcanic cloud is critical in determining its potential hazard and, given that the early stages of evolution are harder to detect (see discussion below), is also important in accurately deriving critical source parameters. An overview is provided in Figure 5.5 (after Turco, 1992).

5.5.1 Opaque clouds

Ash clouds are typically opaque when first erupted, due to the spatially constraining nature of the vent,

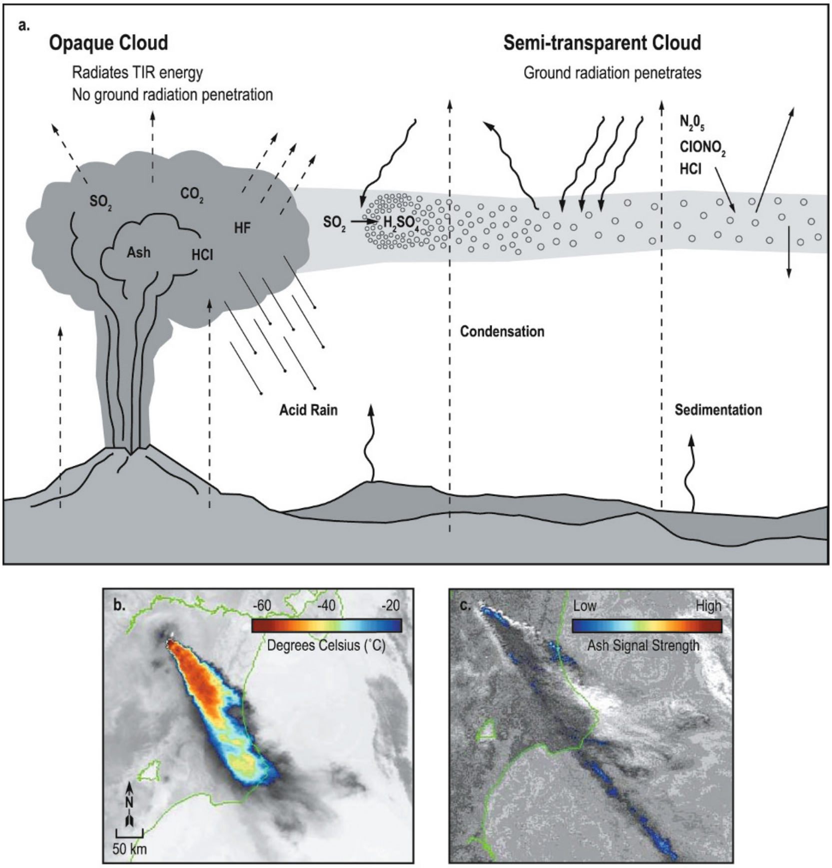

Figure 5.5. A conceptual model and corresponding example of satellite images of a plume. The model (a) shows the structure, composition, and interactions of electromagnetic energy of a typical plume (modified from Turco, 1992). AVHRR images (b) and (c) show the opaque and semi-transparent portions of the plume at Kliuchevskoi Volcano, September 30, 1994. The opaque portions are shown in the TIR (10.5–11.5 μm) image (a) as color-coded for temperature. The BTD image (c) shows the translucent portion of the cloud as a weak ash signal along the edges of the plume (blue) with values ranging from −1 to −2 K.

Table 5.1. The stages of volcanic cloud evolution (after Rose *et al.*, 2000) based on observations of the Mt. Spurr eruption of 1992.

Observable	*Stage 1*	*Stage 2*	*Stage 3*
Duration after eruption stops (h)	1–4	4–24	>24
Fallout (km from volcano)	<25	25–100	>400
Area of fallout (km^2)	<300	$\approx 5 \times 10^4$	Discontinuous
Fallout diameter range (mm)	>0.5	0.5 to <0.01	<0.01
Fallout rate (kg/s)	$>10^4$	$<10^4$–10^2	$\ll 10^2$
Fraction of 1–25 μm (fine) diameter ash (%)	<1	10–50	>50
Cloud area (km^2)	$<10^4$	10^4–10^6	10^6, decreasing
Mean optical depth	>2	0.5–2	<0.3
Cloud ash mass loading (kg/m^2)	>25	2–10	<3
Fraction of suspended material (%)	100–30	30–3	<3

the volume and flow rate of the eruption column, and the fluid dynamical behavior of the ash (i.e., the lack of fallout-associated eruptive thrust). For some time the plume contains a wide range (microns to centimeter-sized fragments) in a limited volume. Satellite measurements of the cloud top temperature at two infrared wavelengths (so-called split-window) are often used to distinguish ash clouds from other types of cloud by making use of brightness temperature differences (BTDs). Although split-window brightness temperature difference retrieval does not distinguish ash without some transmission of terrestrial radiation through the cloud, some information can still be obtained. Given that the cloud is opaque, the satellite will only detect radiation pertaining to the cloud top itself, specifically its temperature using thermal infrared radiance. The cloud must be completely opaque in order to retrieve its approximate radiating cloud top temperature as, otherwise, any derivation will be a function of the cloud's temperature, the ground temperature, and some modulation by the atmosphere between. The cloud's temperature is important as it can be used to determine cloud height. Height is a critical parameter in terms of hazard mitigation and is vital in determining the mass eruption rate. Calculation of the mass eruption rate can be made using the following empirical equation (Sparks *et al.*, 1997):

$$H = 1.67Q^{0.259} \tag{5.1}$$

where H is the column height; and Q is the mass eruption rate in m^3/s. The transition from opaque to transparent cloud has been observed multiple times. The classic example is the Mt. Spurr eruption cloud.

5.5.2 Semi-transparent clouds

Table 5.1 shows the stages of development of a volcanic cloud. Once the cloud becomes semi-transparent it is easier to detect with the split-window algorithm. The transition (from stage 1 to stage 2), a few hours after the eruption finishes, represents the beginnings of detectability of ash clouds using the BTD method, and the first opportunity to retrieve mass, particle radius, and optical depth. Stage 2 is characterized by a coherent drifting cloud, with fallout continuing from smaller particles (and through aggregation). After approximately 24 hours the cloud enters stage 3, where the larger particles have all fallen out and the cloud can be hundreds of kilometers from the source. This often represents the most dangerous phase of the cloud as detection is harder as the cloud thins and the cloud becomes harder to track.

5.6 EFFECTS OF EMISSION PARAMETERS ON SATELLITE DETECTION

Several parameters have a strong control on the ability to detect volcanic ash clouds using satellite instruments with the infrared split-window (also known as brightness temperature difference or reverse absorption) technique. The first is the effective size of the particles in the cloud; there is only a fairly narrow range (1–20 μm, radii) over which the retrieval has sensitivity. This represents the region where Mie scattering and absorption dominate and is related to the ratio of the radius of the particles to the wavelength of the observed radiation, with approximate limits of $(1/2\pi) < x < 2$, where x is known as the size parameter and $x = 2\pi r/l$.

This range represents only a very small fraction of the tephra (and only a small fraction of the total mass, typically <2%) produced during an eruption, although this size range can be suspended in the atmosphere for days and be transported long distances, and therefore can be a serious problem for air traffic. Within the detection limits there is a general trend that smaller particles produce a stronger BTD signal, although the relationship is not simple and is confounded by multimodal size distributions. The effective scattering radius of a particle size distribution is not a particularly reliable metric under these circumstances.

Water vapor in the atmosphere strongly affects the split-window BTD methodology. Much has been published on this effect (Rose *et al.*, 2000; Simpson *et al.*, 2000; Prata *et al.*, 2001; Yu *et al.*, 2002; Pavolonis, 2010), and it is only briefly explained here. The BTD technique relies on the fact that the shorter wavelength of the two bands used (11 μm) is more strongly affected by the presence of volcanic ash than the longer wavelength band (12 μm). This effect is countered by increasing water vapor in the atmosphere where the opposite is true. The NOPAC region represents amongst the best conditions for the algorithm due to the lack of significant amounts of water vapor at higher latitudes.

The silica content of the melt will also have a small, though significant, effect on the signal. Higher silica ash particles absorb more strongly at the shorter end (8–10 μm) of the split-window. All other parameters being equal, increasing the silica content sharpens, strengthens, and narrows the absorption feature (Figure 5.4 after Kearney, 2010) to make it have a more dramatic effect on the split-window channels. Many explosive volcanic eruptions have a higher silica content due to increasing silica which also increases viscosity and, hence, the ability of the magma to pressurize gas.

The height of the cloud also has a significant, though again secondary, effect on the cloud's BTD signal, essentially because height controls temperature and a temperature contrast is required for the retrieval to work. The greater the contrast, the stronger the signal. This is why the retrieval is less sensitive over cold background, as it is possible under some conditions that the cloud and underlying surface temperature are similar or the cloud is warmer than the surface.

5.7 INFLUENCE OF THE ATMOSPHERE ON VOLCANIC CLOUDS

The structure of the atmosphere plays a critical role in the evolution of a plume from its injection to its dispersion. A plume is composed of a turbulent mixture of buoyant hot volcanic particles, gases from the magma, and water or atmospheric gases entrained into the eruption column (Sparks *et al.*, 1997). Condensation, sedimentation, and chemical reactions also occur (Turco *et al.*, 1983) (Figure 5.5). Satellite data are able to detect or measure plume temperature, height, movement, structure, composition, and the transition from opaque to semi-transparent cloud as it drifts away from the source volcano and disperses.

When the volcano first erupts explosively the eruption column is mostly opaque and hot but cools rapidly, usually within a few minutes, as it expands and rises in the atmosphere. The plume rise is due to the initial gas thrust, buoyancy, and vertical convection. As the plume rises it entrains air from the surrounding atmosphere, sheds heat, and becomes less buoyant. When the density equilibrates with the surrounding atmosphere it stops rising (Sparks *et al.*, 1997). Satellite data rarely record the hot phase of the erupting column. As the buoyant plume rises it cools, often to less than −50°C if in the upper troposphere, and is usually opaque (see Figure 5.6). Thermal infrared satellite data are used to detect this stage of the plume and measure its temperature. If the plume is opaque its temperature corresponds solely to material within tens of microns of the cloud top. If it has started to disperse, temperature measurements will include background energy that is transmitted through the cloud resulting in warmer temperature measurements.

The atmosphere consists of four vertical zones with varying thermal structure starting at the Earth's surface: the troposphere, stratosphere, mesosphere, and thermosphere (Figure 5.7). These zones are separated by thermal transitions called

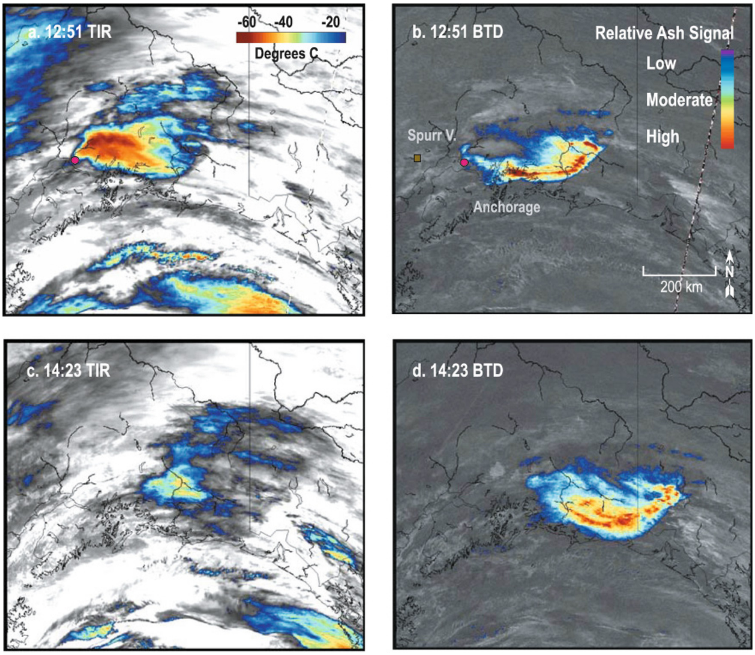

Figure 5.6. Spurr Volcano, September 17, 1992, AVHRR satellite data. These images show the transition from opaque to semi-transparent clouds in TIR (B4, 10–11 μm) and BTD data. The eruption started at 08:03 UTC and the ash cloud was recorded at 12:51 in B4 (a) and in BTD data (b). By 14:23 UTC the signal has changed as seen in B4 (c) and the BTD data (d). At 12:51 the B4 image (a) shows an opaque cloud northeast of Anchorage which is color-coded by temperature in orange and red. The temperature signal along the eastern edge of this cloud is warmer suggesting an increase in contribution from the ground beneath the cloud. In the same area the BTD data (b) show an increase in the ash signal. No ash signal is detected on the BTD image at the opaque portion of the cloud due to its opacity. At 14:23 the opacity of the plume decreased as dispersion increased (c) and the BTD signal of the ash cloud is stronger (more negative) (d).

the tropopause at 11 km, stratopause at 47 km, and mesopause at 81 km based on a standard atmosphere (Lutgens and Tarbuck, 1995). (Note that these boundaries vary in space and time and are not fixed; the values given are illustrative only.)

In recent times the highest plumes were from eruptions of Mt. Katmai which ascended to 30 km (Fierstein, 2007), Mt. St. Helens to 30 km (Holasek and Self, 1995), and Mt. Pinatubo to 40 km (Lynch and Stephens, 1996). Comparing the maximum height of these plumes with the structure of the atmosphere shows that they are below the stratopause boundary (Figure 5.8). The thermal structure of the atmosphere defines the atmospheric zone boundaries (Figure 5.7). The tropopause has a negative temperature gradient, warmest at the Earth's surface and coolest at approximately −60°C at the tropopause boundary, near 11 km, in this example. The tropopause is the boundary where the atmospheric temperature gradient becomes positive or remains close to zero; above lies a region called the lower stratosphere with temperatures at approximately −60°C and warming to approximately 0°C at the stratopause, near 47 km, in this example. Usually, the tropopause and stratopause boundaries are not abrupt thermal reversals—but have fluctuating temperatures of a few degrees about or near the thermal gradient inflection point. These regions of fluctuating temperatures at the tropopause, stratopause, and mesopause can be 10 km thick. In addition, the tropopause is weakly stratified while the stratosphere is intensely stratified, especially at heights above 20 km. Thermal reversals and stratification in the atmosphere hinders the ascent of plumes. When a plume encounters the tropopause, temperature reversal changes the buoyancy conditions and slows or stops its ascent. Only more energetic erup-

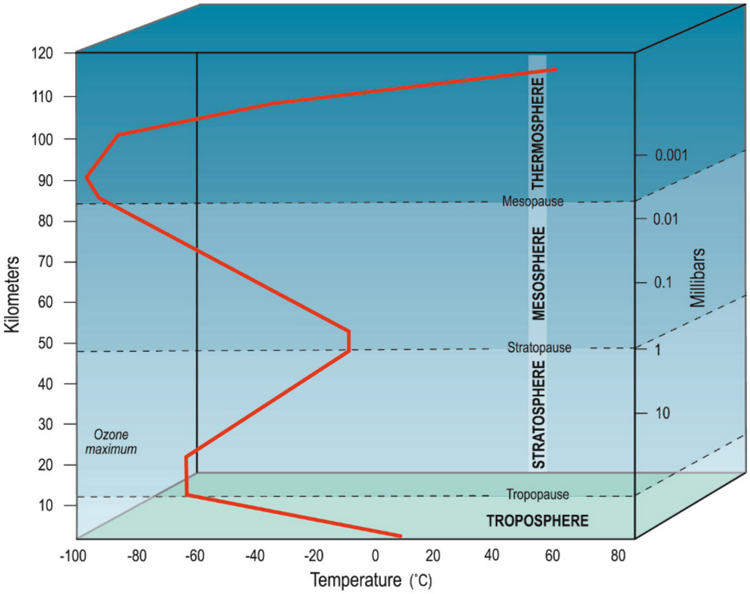

Figure 5.7. The basic thermal structure of the atmosphere is defined by temperature gradients as a function of altitude which reverse at three different levels. The pressure decreases with increasing altitude. The temperature gradients and pressure impact how a plume rises and its maximum height as it equilibrates to surrounding conditions. There are no records of a volcanic plume penetrating the stratopause. The tropopause stops or slows the rise rate of less energetic plumes where they tend to spread laterally.

tions produce plumes that are able to penetrate the tropopause and enter the stratified layers of the stratosphere (Sparks *et al.*, 1997), such as Redoubt (2009), Kasatochi and Okmok (2008), Augustine (2006), Mt. St. Helens (1980), and Katmai (1912). Most of the eruptions in the North Pacific region are unable to penetrate the tropopause, and if they do get to that height they tend to spread laterally. Modern-day jet aircraft fly at heights of 10 to 12 km which is above the tropopause but still at levels of drifting ash clouds. Ash clouds below the tropopause are a threat to local air traffic and surface infrastructure (Figure 5.8).

The height of the tropopause is not fixed but varies as a function of latitude and time. In tropical regions the boundary is 16 to 18 km, and temperatures increase sharply above this resulting in a very stable stratified atmosphere. In mid-latitudes the tropopause is about 11 km, the temperature remains fairly constant to about 20 km, and the atmosphere becomes even more stratified. In polar regions the tropopause is located at about 8 km and the atmosphere is less strongly stratified than in the tropical and middle latitudes. The tropopause tends to be a little higher, such as 10 km during the summer in polar regions (Sparks *et al.*, 1997). Due to variations in the height of the tropopause, plumes from tropical eruptions that do not have enough energy to penetrate the boundary attain greater altitudes than those in polar regions, assuming that they have similar buoyancy.

Other factors that impact plumes include atmospheric pressure, density, and water vapor density (Table 5.2). A plume will continue to rise until it comes into static equilibrium with its surrounding environment (although oscillations about and overshooting of this level also occur). A plume will be in equilibrium with its surrounding environment when the density of the plume equals the density of the surrounding environment. The density of both the plume and surrounding environment depends on the temperature, pressure, and water vapor loading. Initially, the eruption column is unsaturated but, as the column ascends, it entrains surrounding air, including moisture, and becomes saturated at approximately 8 km. Above 8 km the air pressure and moisture content is low. The heights attained by small plumes are greater in the tropics due to the moist atmosphere compared with those in the dry atmosphere in polar regions. Generally, plumes

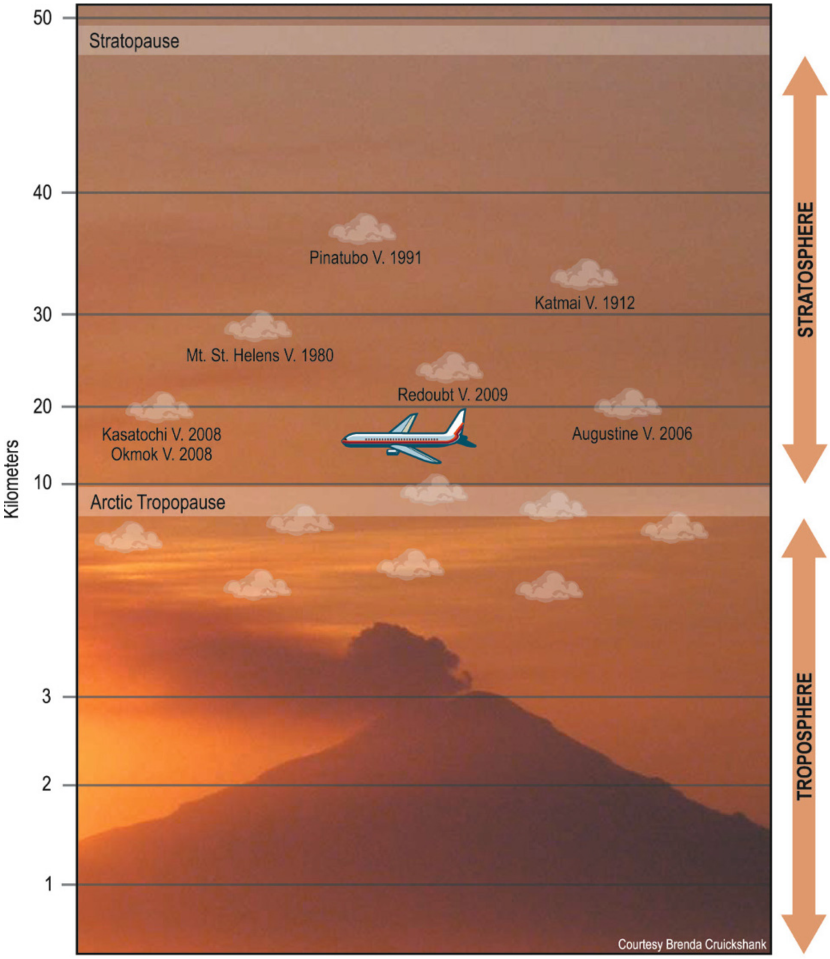

Figure 5.8. Relationship between the structure of the atmosphere, plume heights, and air traffic. Only very energetic plumes can ascend into the stratosphere, where the atmosphere is extremely stable and does not easily support vertical convection. Often an eruption will be composed of numerous plume-producing events but only the more energetic and hence dangerous plumes have sufficient energy to penetrate the tropopause. A few examples of stratospheric eruptions are shown. The weaker plumes from volcanic activity do not make it to the tropopause or are prevented from ascending beyond that boundary. Jet aircraft often fly at altitudes between 9 and 12 km, heights that energetic plumes ascend to or pass through.

Table 5.2. Generalized examples of physical values of the atmosphere at the surface, tropopause, and mesopause based on a standard atmosphere (Lutgens and Tarbuck, 1986).

Height (km)	*Temperature* (°C)	*Pressure* ($kg\,m^{-3}$)	*Air density* ($g\,m^{-3}$)	*Water vapor density*
Surface	15	1,000	1.22	8
11	−60	265	0.414	0
47	−5	2	0.004	0

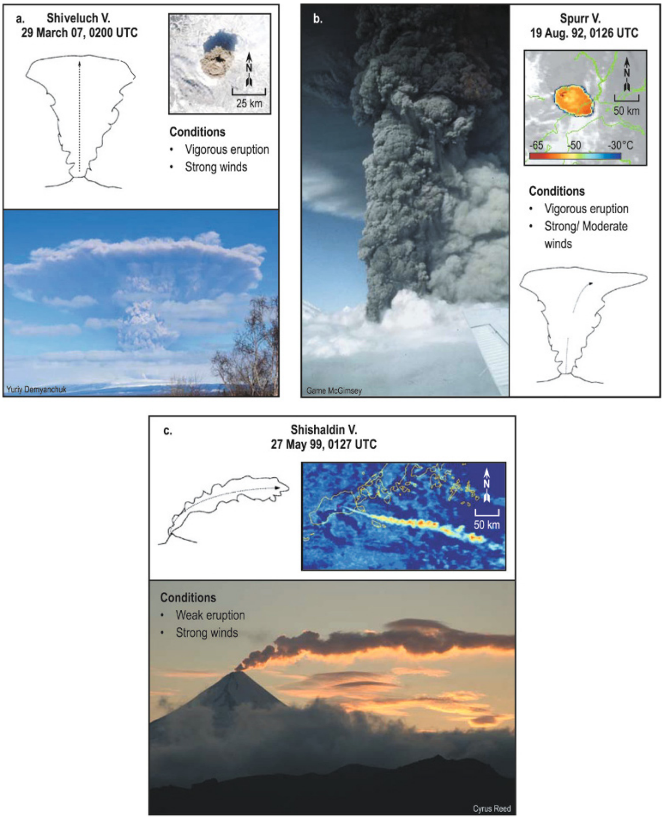

Figure 5.9. The relative effect of wind and eruption vigor shown as conceptual models (modified from Sparks *et al.*, 1997). The eruption of Shiveluch Volcano (a) shows a circular umbrella cloud above a vigorous eruption column. The MODIS color composite satellite image shows a plume and its shadow on snow-covered ground. The plume top height is 14 to 15 km with a wind speed of 13 to 15 m s^{-1} blowing to the NNE at that height. Even though the plume encountered strong winds, the highly energetic eruption resulted in a high-altitude circular plume. The eruption of Spurr Volcano (b) shows an elliptical-shaped high-altitude umbrella cloud above a vigorous eruption column. The plume top height is 14 km with a wind speed of 13 m s^{-1} blowing to the ESE at that height, elongating the plume. The AVHRR satellite image is TIR B4 which has been color-coded by temperature and recorded 31 min after the start of the eruption. The eruption of Shishaldin Volcano (c) shows a weak eruption column in high-velocity winds (13–15.5 m s^{-1}), resulting in a low-altitude bent-over plume, extending approximately 400 km to the ESE at a height of 4 km. The AVHRR satellite image is processed to detect ash clouds using the BTD technique.

whose height exceeds 12 km are not significantly impacted by atmospheric moisture (Sparks *et al.*, 1997).

Wind direction and strength impact the shape of a plume and the dispersal of ash and gas for both large and small plumes (Figure 5.9). If wind was not present then both small and large plumes would rise vertically above the source vent and spread radially forming an umbrella cloud once the neutral buoyancy height is reached or they would dissipate. A profile view of large vigorous plumes would show that the vertical axis of the eruption column will be bent in the downwind direction and the umbrella cloud will be distorted in that direction (Sparks *et al.*, 1997). From a satellite perspective only the umbrella cloud can be observed but its shape would be elliptical instead of circular with its center displaced downwind from the position of the source vent. A profile view of small weak plumes would show a long and narrow column bent downwind. From a satellite perspective a long and narrow plume extending downwind would be observed.

Dispersion of the plumes can be mapped using high temporal resolution time-sequential satellite data such as from the GOES imaging sensor where TIR data is recorded every half hour. These images provide a snapshot in time—but not predictions of its movement. The use of gridded wind fields that include predictions of wind direction and speed in dispersion models are used to predict the movement of ash and gas clouds, which is especially useful for hazard mitigation (Searcy *et al*., 1998). (See Chapters 7 and 9 for a more detailed discussion of dispersion modeling and its use. Animations of ash movement using dispersion models can be seen on the DVD).

5.8 CLOUD HEIGHT ESTIMATIONS

Estimating the height of plumes and ash clouds is one of the most critical components for hazard response in the North Pacific region. The height of the cloud dictates how the wind fields control movement, and this impacts how agencies and industry (especially airlines) respond to an eruption. Erroneous height estimates can result in an incorrect hazard response, such as invalid forecasts of ash cloud movement that could potentially be catastrophic. There are several quantitative methods for estimating plume and ash cloud heights: temperature, trajectory, shadow, stereoscopic, and radar. Ground observers and pilot reports (PIREPS) provide qualitative estimates. Measurements from each method do not always agree, so heights are only estimates; each method has its strengths and weaknesses. At this time, ground-based radar appears to be the most accurate and dependable method for estimating height near the vent where the particles are large enough to be detected by radar.

5.8.1 Temperature method

The temperature method involves comparing the cloud top temperature with the temperature profile of the atmosphere and requires that the cloud be opaque and the temperature equilibrated to the surrounding atmosphere. If the cloud is semi-transparent the measured temperature will include radiant energy from the underlying background, and this usually increases the measured cloud temperature resulting in an erroneously low height estimate. The most accurate cloud temperature is measured using satellite data in the 11 μm TIR band (Sparks *et al*., 1997; Dean *et al*., 2004). The plume temperature is then correlated to the temperature–height profile of the atmosphere measured by radiosonde launches from airports. Ideally, there is only one temperature that correlates to one altitude unless the plume penetrates the tropopause; in those situations usually several heights will be associated with the same temperature. For example, the eruption of Spurr Volcano on August 19, 1992 was recorded on over 11 satellite images for 83.4 hours (Figure 5.5) showing the evolution of the cloud from opaque to semi-transparent (Schneider *et al*., 1995). The cloud remained mostly opaque (Figure 5.10) for ~5 hours with a fairly consistent temperature ranging from −65°C (01:26 UTC), −61°C (03:31 UTC), and −63°C (05:12 UTC). These temperatures correlate to heights ranging from 11.5 to 12 km. Ground-based radar showed a height of 13.7 km (Rose *et al*., 1995). Augustine Volcano at 01:40 UTC on January 14, 2006 is an example of multiple height estimates, as well as of the evolution of an opaque to semi-transparent cloud and its effect on temperature measurements (Figure 5.11). The first TIR B4 satellite image recorded at 01:45 UTC showed an opaque cloud with temperature of −53.5°C which correlates to height estimates of approximately 8.0 and 9.5 km which straddle the tropopause at 8.5 km. Ground-based radar indicates a height of 10.5 km and pilot reports indicate 9 to 9.5 km (Bailey *et al*., 2010). All of these estimates are in the vicinity of the tropopause. A few hours later TIR B4 images recorded at 02:43 and at 03:27 UTC (Figure 5.11c, e) showed minimum cloud temperatures of −49.5 and −40°°C, respectively, which are warmer than the cloud at 01:45 UTC and correlate to a much lower height. The plume temperature increase is almost always due to thermal contamination from the warm background indicating that the cloud has begun to disperse and is now semi-transparent. Brightness temperature difference (BTD) images (Prata, 1989a) of the cloud at 02:43 and 03:27 (Figure 5.11b, f) show an ash signal that is also indicative of a semi-transparent cloud. As shown above and discussed by others (Tupper *et al*., 2004), height estimates are subject to error from limitations of the technique.

The location of temperature profiles from radiosonde measurements used to identify heights can also be problematic. The profiles are generated at selected airports—not at volcanoes themselves. The profiles can be located hundreds of kilometers from a volcano and may not provide a temperature profile that is representative of that above the

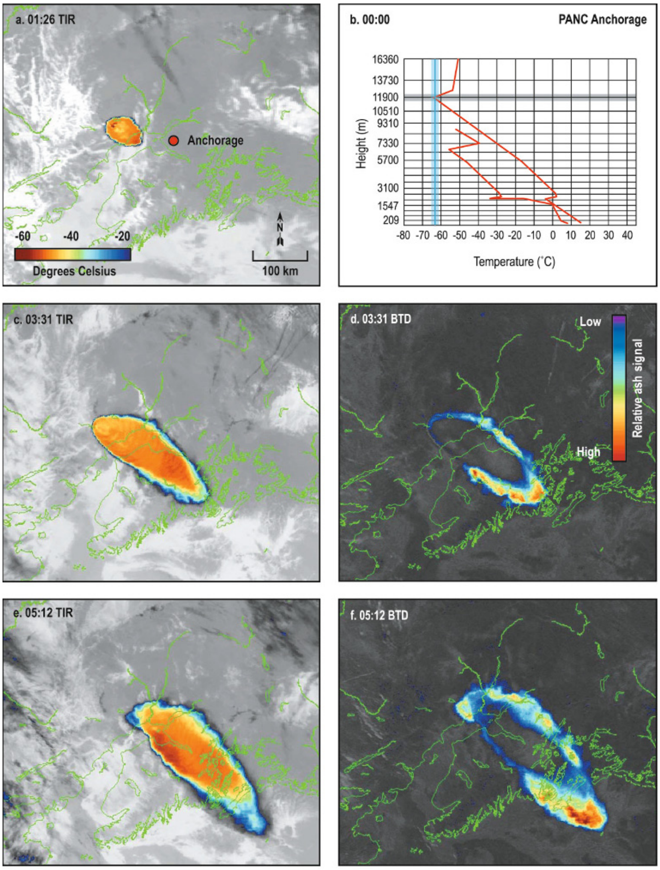

Figure 5.10. Mt. Spurr Volcano erupted on August 19, 1992 at 00:55 UTC recorded on AVHRR satellite images at 01:25, 03:31, and 05:12 UTC and show the early stages of the transition of this plume from opaque to semi-tansparent. Images (a), (c), and (e) are TIR B4 (10–11 μm) data. Images (d) and (e) are BTD data. The single TIR band data show an opaque cloud at 01:26 UTC (a) with a temperature of −65°C. The dry atmospheric profile (b) shows the thermodynamic tropopause to be at 12 km (gray line) and the atmosphere and plume temperature that corresponds to that height (blue line). Images (c) and (e) recorded at 03:31 and 05:12 UTC show the opaque cloud starting to become semi-transparent along the edges of the BTD data (d) and (f). There is no negative BTD signal in the core area of the cloud, because that area is still opaque. The lack of a BTD signal suggests that the cloud temperature is not contaminated with background temperatures. The UTC time is shown on the images.

volcano. A solution to the problem is the use of gridded atmospheric models (e.g., UNIDATA) to generate profiles above a volcano. Presumably, these would be more accurate than distant sounder measurements. A comparison of rawinsonde and modeled profiles has not been systematically evaluated but qualitative comparisons suggest that these are reasonable estimates.

Another problem complicating plume temperature measurements are supercooled portions of plumes that are highly buoyant, also referred to as the dynamic overshoot (Woods and Self, 1992; Holasek and Self, 1995). The material in the convective column ascends until it reaches its neutral buoyancy but, due to inertia, it is carried farther upward. After the inertia has dissipated, this overshoot descends to its neutral buoyancy position in the umbrella cloud probably within minutes (Sparks *et al.*, 1997). In this situation the overshoot is the coldest part of the cloud—even colder than the surrounding atmosphere—and would therefore not be used to estimate its height. Usually, the over-

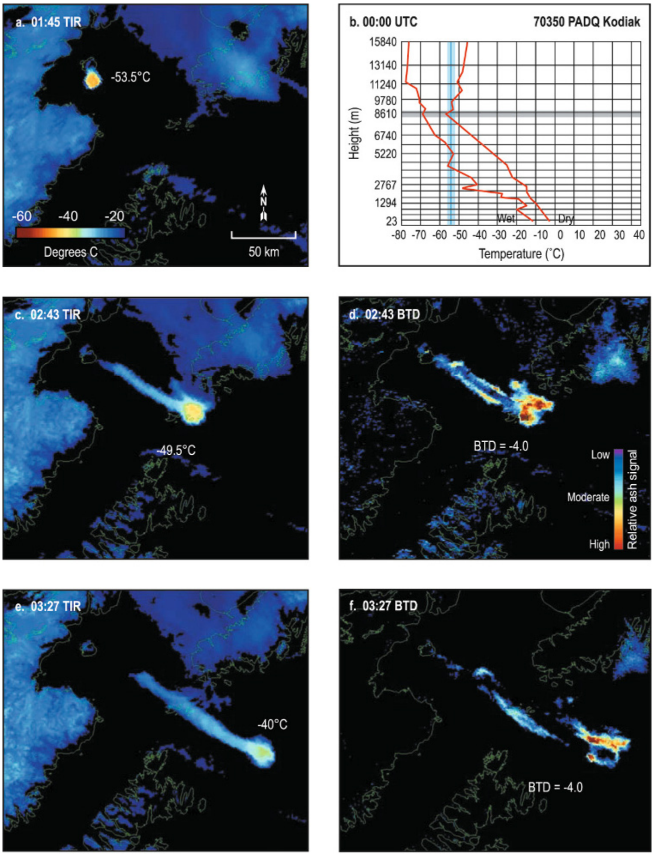

Figure 5.11. Augustine volcanic eruption in January 2006. AVHRR images recorded on January 14, 2006 show how the morphology of a volcanic cloud changes over time and impacts height estimates. Images (a), (c), and (d) are B4, (d) and (e) are BTD, and (b) is the atmospheric temperature profile. At 01:45 UTC (a) an opaque cloud is observed with the coldest temperature of −53.5°C, the blue line in (b). This cloud correlates to a height of 8.0 and 9.5 km which straddles the tropopause at 8.6 km, the gray line in (b). At 02:43 (c) and 03:27 (e) the TIR data show that the coldest temperature of the cloud has increased to −49.5 and −40.0°C, respectively. These same images processed for BTD (d) and (f) show a relatively strong BTD signal of −4.0. The increasing cloud temperature and strengthening BTD signal is indicative of a dispersing cloud and conducive to the detection of ash. Ground-based radar measured a height over 10.5 km at 01:40 UTC and PIREPs reported 9.0 to 10.5 km. The cloud is moving to the southeast which correlates to wind fields in the atmospheric profile data at heights less than ~9.5 km (see Section 5.9.2). The variations in height estimates show the difficulty in precise height measurements of dynamic volcanic clouds.

shoot is above the convective column and still connected to the vent. To estimate the height of these clouds the coldest temperature in the umbrella cloud, excluding the overshoot, should be measured and compared with the atmospheric profile (Dean *et al.*, 1994). An example of a supercooled plume observed on satellite data is the eruption of Redoubt Volcano, January 8, 1990 (Figure 5.12). The satellite image was recorded at 19:11 UTC, 13 minutes after the start of the eruption. In this example the plume is circular with a diameter of approximately 40 km. The bright-red portion is the overshoot at −63°C while the coldest atmospheric temperature (Anchorage radiosonde) is approximately −55°C (Figure 5.12b). A temperature profile (Figure 5.12c) across the plume shows a low temperature of −63°C approximately at the center (topographically high), a warmer tempera-

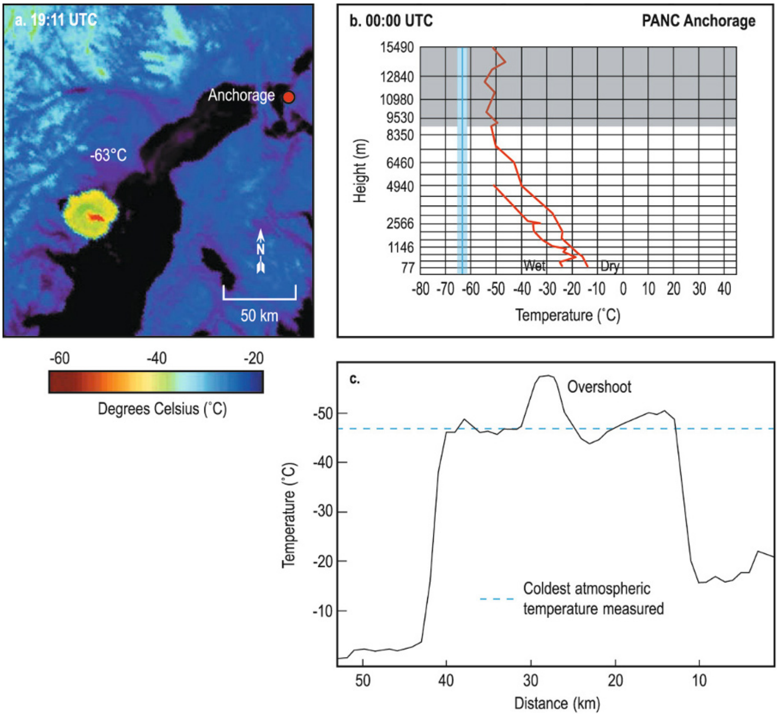

Figure 5.12. Height estimates of the Redoubt Volcano plume on January 8, 1990 recorded on TIR (11 μm) AVHRR data (a) at 19:11 UTC, 13 min after the start of the eruption. The plume is color-coded by temperature with the coldest temperature, −63°C, shown as the blue line in (b). The coldest atmospheric temperature recorded on the radiosonde profile (b) is −55°C at 12.5 km. Therefore, the red portion of the plume has overshot its neutral buoyancy level as shown in the temperature profile of the plume (c). The portion of the plume that appears to be neutrally buoyant has a temperature of −51°C, the dashed line in (c), and correlates to an estimated minimum height of 8.5 km based on the atmosphere temperature profile. Within a few minutes the overshoot will settle to its neutral buoyancy level probably with a temperature of approximately −55°C at 12.5 km. Previous height estimates (Dean *et al.*, 1994) range between 9–11 km and differ due to the radiosonde profiles that were used. Heights greater than 12 km have also been estimated for this eruption (Miller and Chouet, 1994).

ture trough (−44°C) surrounding the overshoot, and a cold (−51°C) topographically elevated rim. The estimated height of this plume using the temperature method is 9, 11, or 15–17 km.

The temperature method has several limitations as shown above but is a technique that often provides a first-order estimate until additional information becomes available. The limitations include multiple heights for the same temperatures, supercooled portions of plumes, masking by weather clouds, and invalid cloud temperatures due to contamination from background signals.

5.8.2 Trajectory method

Trajectories can be used to estimate cloud heights whenever there is vertical wind shear in the atmosphere. The basic idea is to use a trajectory/dispersion model initialized using atmospheric wind data and guessing the starting height of the volcanic cloud. The resulting trajectory can be compared with a satellite observation and iterated by changing the starting height until a best fit is obtained. This process can be mathematically formalized to obtain an initial height distribution of the erupted mass (see Stohl *et al.*, 2011).

The eruption of Kliuchevskoi Volcano on September 30, 1994 is an excellent example (Figure 5.13). A satellite image recorded at 20:54 UTC shows a bifurcated plume blowing to the southeast with a segment appearing to loop beneath another segment. The Puff dispersion model shows that the lower portion of the plume is at an altitude of 4 to 8 km and the upper portion is at 8 to 12 km. The

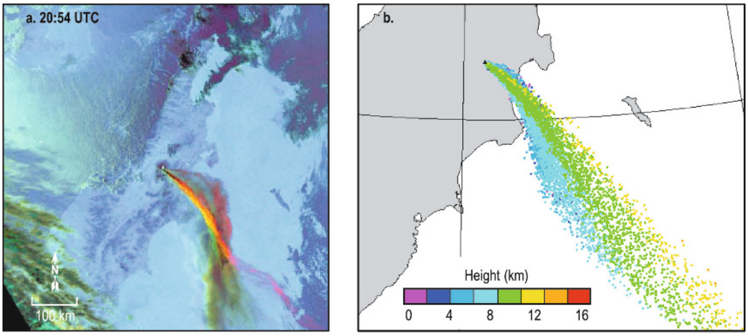

Figure 5.13. Estimation of plume height using the trajectory method for an eruption of Kliuchevskoi Volcano, September 30, 1994 at 20:54 UTC. The AVHRR color composite image (a) shows a bifurcated plume with a segment blowing southeast over the top of another segment blowing south-southeast. The Puff dispersion model (b) shows that the southeast segment (green and yellow) is at 8 to 12 km altitude and the south-southeast segment (blue) is 4 to 8 km.

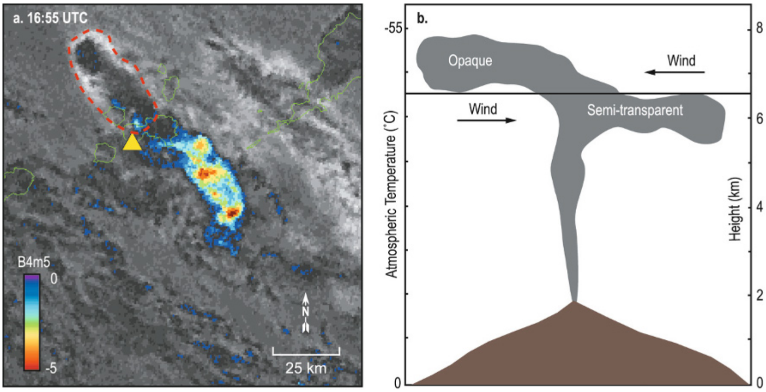

Figure 5.14. A composite of AVHRR satellite images (a) using TIR and BTD data and the conceptual model (b) shows an early stage of a volcanic cloud at Cleveland Volcano, February 19, 2001 at 16:55 UTC. The NW portion of the plume is opaque (dashed polygon) and detected on single-channel thermal infrared (TIR) B4 data with the coldest radiant temperature of −53°C, which correlates to an altitude of 8 km. The SE segment of the cloud is semi-transparent and detected on BTD data with a signal strength less than −5. The wind shear indicated in the Puff dispersion model suggests that the SE volcanic cloud is at an altitude of approximately 6.5 km (after Dean *et al.*, 2004). Wind directions are relative to Cleveland Volcano (yellow triangle).

eruption of Cleveland Volcano on February 19, 2001 (Dean *et al.*, 2004) is an example of the separation of the opaque and semi-transparent ash cloud due to wind shear. The temperature and trajectory technique had to be used to estimate heights and analyze the structure of the cloud (Figure 5.14). The TIR (10.5 μm) channel of an AVHRR satellite image recorded at 16:55 UTC showed an opaque cloud northwest of the volcano at a temperature of −53°C, which indicates a height of 8 km. However, further analysis of the satellite data using the BTD technique revealed that there was also an ash-rich, semi-transparent cloud (not detected in the single-band TIR image) southeast of the volcano. Ash trajectory predictions using the Puff dispersion model indicated that there was directional wind shear at a height of approximately 7 km blowing to the southeast indicating that the ash cloud was at a height below 7 km. A conceptual model of the structure of the cloud shows how the cloud is sheared at 7 km (Figure 5.14b).

Trajectory-based height estimates have a few limitations. Directional or velocity wind shear must be present for this technique to work, and the accuracy of the dispersion model depends upon the accuracy of the atmospheric data and gridded wind models. One of the most troublesome regions on a planetary scale is the lower 3 km of the atmosphere, in the region known as the planetary boundary layer (PBL) where turbulence dominates. Above this region, in the free atmosphere, turbulent effects can be mainly ignored in an approximate treatment of synoptic-scale motions (Holton, 2004). However, due to the height of volcanoes and the effects of an explosive eruption, the turbulence can extend a few kilometers higher in the vicinity of a volcano. The capability of gridded wind fields to accurately portray the PBL layer is variable between models. Thus, ash dispersion models at these low altitudes can be problematic. (See Chapter 7 for a more detailed discussion of dispersion models.)

5.8.3 Cloud shadow method

The cloud shadow method involves geometric principals based on the relationship between plume height and the solar elevation angle (Holasek and Self, 1995); $h = d \tan q$. Here h is the height of the plume, d is the shadow length, and z is the solar elevation angle measured from the horizontal (Figure 5.15). The length of the shadow is measured on satellite data using a visible light band from the highest part of the plume which in most cases is above the volcano to the outer edge of the shadow. The tangent of the solar elevation angle (θ) is measured at the ground intersection. Simple multiplication of the tangent of θ and the distance gives an estimate. In this example a flat Earth is assumed. Greater accuracy can be attained if the curvature of the Earth is taken into account but this complicates the calculations significantly. This method has several limitations and potential sources of error that hamper its use. It requires daylight for the shadow to be formed (a problem during the long winter nights at high latitudes), the Sun must illuminate the plume obliquely, and the satellite must be in a location that permits viewing the shadow. Definitive identification of the end of the shadow can also be a problem when other shadows are present or the night terminator is in the general area. Large satellite pixels such as those in the GOES data at high latitudes can vary by a few kilometers and, thus, are not conducive to precise measurements.

5.8.4 Ground-based radar method

Ground-based radar is a relatively new technique for estimating the height of volcanic ash and is quite

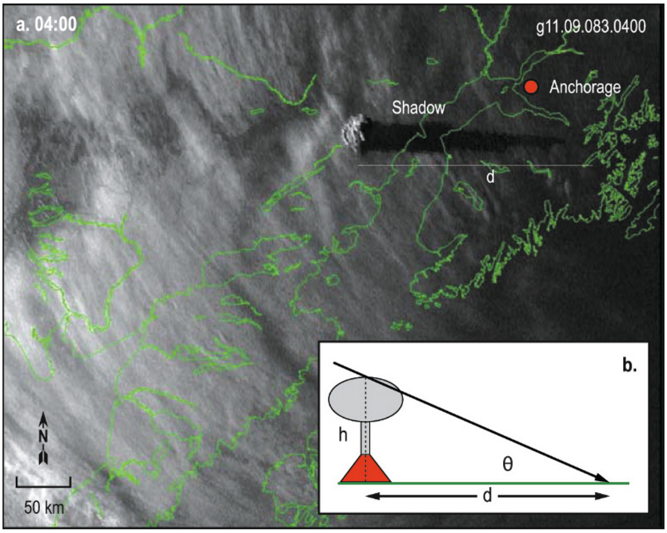

Figure 5.15. A GOES satellite image (a) recorded in the visible shows a plume from the eruption of Redoubt Volcano, March 24, 2009, 04:00 UTC. The height (h) of the plume is estimated based on the shadow length (b) and solar zenith angle (θ) where $h = d \tan q$. The length of the shadow (250 km) is measured on the satellite image, the solar zenith angle is 3°, and the resulting height is 12 km (40,000 ft.).

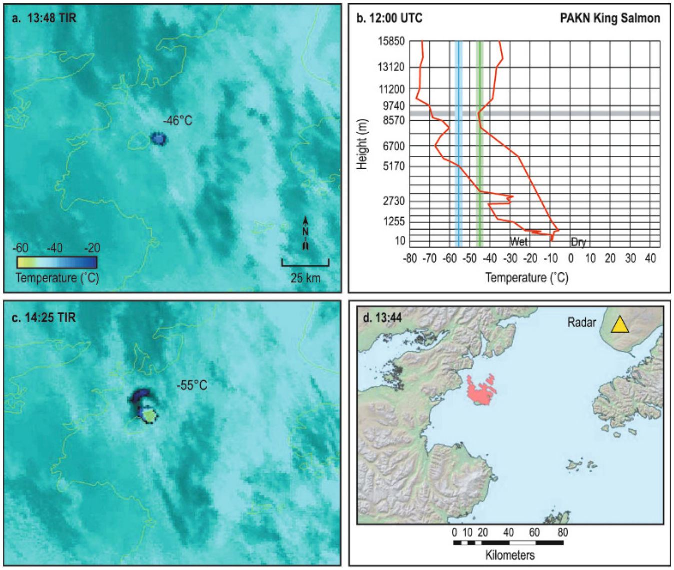

Figure 5.16. Example of plume height estimates from ground-based radar and temperatures at Augustine Volcano, January 11, 2006. Two eruptions occurred at 13:44 and 14:12 UTC. The satellite image (a) recorded at 13:48 UTC, 4 min after the first eruption, shows an opaque plume with a temperature of −46°C, the green line in (b), which corresponds to two altitudes of 7.5 and 12 km based on radiosonde data (b). A second satellite image at 14:25 UTC (c), 13 min after the second eruption started, shows a temperature of −55°C, the blue line in (b), which suggests the plume is supercooled since it is colder than the dry radiosonde profile. Ground-based radar (not shown) measured 9 km at 13:44 UTC. The tropopause, the gray line in (b), is at a height of approximately 9.1 km. A composite of radar data (d) recorded at 13:49 and 15:31 UTC shows the plan view of the particles which generally matches the location and shape of the plume observed on satellite data.

reliable when the size of the particles is large enough to be detected. The active system transmits microwave energy towards the eruption cloud which is then reflected back to the instrument by particles that are encountered. The instrument receives and processes the data which are then displayed as echo intensity (reflectivity) measured in dB (decibels). Radar energy is reflected by particles such as ash, precipitation, and ice crystals—but not gases. Radars can be operated in several ways, such as clear air or precipitation mode (affects sensitivity), and can generate a variety of products applicable to volcanic ash detection: plume top height, plan view of maximum reflectivity, and vertical or horizontal cross-sections of reflectivity (Figures 5.16 and 5.17). The temporal resolution of the scans is measured in minutes which provides unprecedented looks at the formation and collapse of eruption columns. Typical radar wavelengths used by these systems are the S, C, and X-bands. The size of ash particles detected by radar are fine (large volume <10 μm), coarse (10–64 μm), and lapilli (>1 mm) (Rose *et al.*, 1995; Marzano *et al.*, 2006; Wood *et al.*, 2007). In the North Pacific region there are several ground-based radar instruments available (in Alaska and the Cascades). Most are the S-band Weather Surveillance Radar (WSR-88D, the "D" standing for Doppler) for monitoring weather but have been successfully used to detect volcanic ash (Wood *et al.*, 2007). The WSR radar is part of the U.S. next-generation radar (NEXRAD). The maximum range of this radar is approximately 220 km. There is also a transportable C-band instrument operated by the USGS that is dedicated to volcano monitoring (pers. comm., D. Schneider, USGS AVO) and built by Enterprise Electronics Corporation (MiniMax 100C). The maximum range of the USGS radar is 100 km. In the Cook Inlet region the WRS-88D and USGS instruments are located near Kenai (Alaska) providing coverage of the most active volcanoes in that area. There is no radar coverage for Aleutian volcanoes, but since the USGS radar is transportable it could be moved to provide coverage for other areas. In the Cascades WSR-88D instruments are

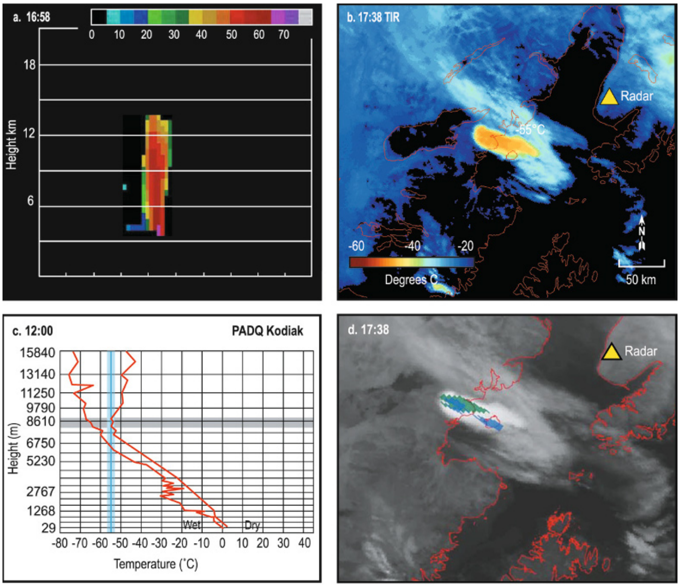

Figure 5.17. A wide range of plume heights were measured for the eruption of Augustine Volcano on January 17, 2006 at 16:58 UTC. A height of 14 km was measured by ground-based radar as shown in a profile view of the plume (a) at 16:58 UTC. An AVHRR satellite image (TIR, B4) recorded an hour later (b) shows a minimum plume temperature of −55°C which correlates to an altitude of 8 km based on the atmosphere profile, the intersection of the blue and gray line in (c). The tropopause height, the gray line in (c), equals 8 km. The height of ash particles detected on the plan view of radar (d) coincides with height estimates from radar data (a), 3.8 km (green) and 7.2 km (blue).

located at many cities in Washington, Oregon, Idaho, and California, providing coverage of most volcanoes in the region. In the Kamchatka Peninsula and the Kurile Island regions there are no civilian radars available for coverage of volcanoes at this time (pers. comm., P. Izbekov, UAF AVO).

One of the earliest applications of ground-based radar for volcanic eruptions was in Iceland at the 1970 eruption of Hekla Volcano (Marzano *et al.*, 2006). Others include Mt. St. Helens, 1980 (Harris and Rose, 1983; Harris *et al.*, 1981); Mt. Spurr, 1992 (Rose *et al.*, 1995); Hekla Volcano, 2000 (Lacasse *et al.*, 2004); Mt. Augustine, 2006 (pers. comm., D. Schneider, USGS, AVO); and Mt. Redoubt, 2009. Radar has been used to detect ash for at least 24 eruptions worldwide (Marzano *et al.*, 2006). These and other studies suggest that radar plume height estimates appear to be more reliable and consistent than the other methods described above, but some dilemmas were encountered. Radar provides discrete estimates even in the tropopause where the cloud temperature method has problems. For example, height estimates from satellite images of the first eruption on January 11, 2006 at Augustine Volcano were not definitive (Figure 5.16) because the plume penetrated the tropopause but the radar showed 9 km. Height could not be estimated for the second eruption since the satellite temperature of the plume was colder that the radiosonde profile (Figures 5.16b, c). Radar measurements were not available for this second eruption. However, using a wet adiabatic lapse rate of −4.5°C/km, based on a lapse rate calculated from the radiosonde and a base temperature of −10°C also from the radiosonde profile (Figure 5.16b), the height was estimated to be 10 km. A plan view derived from the composite radar images over this period corresponds in space and time with the satellite images. During the Augustine eruption on January 17, 2006 at 16:58 UTC, the plumes penetrated the tropopause, which resulted in height estimates ranging from 6.5 to 13.5 km. Radar showed 14 km, which was close to the upper temperature estimates (Figure 5.17). For the many explosive events at Augustine 2006, the height estimates were both higher and lower than the satellite estimates but usually within a few kilometers (Bailey *et al*., 2010). During the Redoubt 2009 eruption preliminary radar estimates showed some cloud tops over 18 km while satellite temperatures indicate heights near the tropopause (9.5 km). Moreover, movement of the ash clouds is consistent with dispersion model predictions at the lower altitudes. Perhaps the bulk of the Redoubt ash is near the tropopause boundary, which is what the satellite detects but the concentration of the higher material may be below satellite detection limits for ~1 km^2 pixels. Another dilemma is the rapid rise rate of these very high cloud tops, 400 m s^{-1} at Mt. Pinatubo (Oswalt *et al*., 1996), which exceeds the typical rate of a few tens to 200 m s^{-1} (Sparks *et al*., 1997). Similar or even higher rise rates were calculated at Redoubt (2009). Perhaps the high rise rate is related to a pressure wave caused by the eruption and to condensing clouds behind the wave, which is what radar may be detecting (pers. comm., C. Cahill, UAFGI). Resolution of the large height discrepancies between radar and satellite measurements is critical for accurate hazard warning and assessment and will require further study.

Ground-based radar offers significant advantages over other techniques for measuring plume height and collecting additional information about an eruption, but there are limitations. Advantages include accurate height and position estimates in near-real time, high temporal resolution measurements of ash rise and fall rates, ash retrieval (mass), and gas cloud penetration. All of these advantages are critical measurements for hazard assessments. Disadvantages include the limited number of volcanoes within radar range, detection limited to coarse particles or high concentrations of fine particles, and detection limited to ash near the vent where larger particles are still airborne compared with distal volcanic clouds that contain finer particles. Radar is most sensitive to large particles; the returned power is proportional to r^6. The thermal BTD signal arises from small-sized ash particles ($r < 16\,\mu\text{m}$). Radars are also expensive to purchase and maintain, requiring significant manpower. These limit availability in many parts of the world.

5.8.5 Stereoscopic methods

Several satellite sensors include the capability to image the same scene from multiple view angles simultaneously, or from different view angles within a short time, or from different view angles using two or more platforms. Among these are MISR, the ATSR family, and by using two or more geosynchronous satellites. The principle of stereoscopic imaging is well established (Hasler, 1981; Wylie *et al*., 1998; Glenkova *et al*., 2007) and needs no further discussion here. A recent study by Scollo *et al*. (2010) employed MISR imagery to estimate plume tomography for the 2001 Etna eruption. Prata and Turner (1997) have shown how the conical scan of the ATSR instrument can be used to determine cloud top height by combining two views, one at 22° and the other near 55°, in either infrared or visible channels. Since these methods are essentially geometrical, the limitation is largely due to the pixel size (1 km in the case of the ATSRs) and to the skill and sophistication of the pattern-matching techniques employed. The method is not restricted to daytime-only use as pattern-matching can be done using the infrared channels. For the NOPAC region stereoscopic height estimation can be done using data from two geosynchronous measurements (see Hasler, 1981 for details on the methodology), giving the possibility of high temporal resolution cloud height estimates.

5.8.6 Pilot reports

Reports from pilots (PIREPS) or ground observers are a qualitative observation but still an important contribution to height estimation. Often these are the first estimates, especially in remote areas, where satellite and radar data are limited or not available. Because of their qualitative nature the variance can be large, depending on the experience and thoroughness of the pilot. (Examples of two of these eruptions are shown in Figures 5.16 and 5.17; see Chapter 9 for more details.)

5.8.7 Comparing height estimates

Plume height estimates can be quite variable between different techniques and may differ by many kilometers. Height estimates from the eruptions of Augustine Volcano, 2006 (Bailey *et al*., 2010) exemplify variations in the different techniques (Table 5.3). These eruptions emitted plumes that ascended to heights less than, equal to, or above the tropopause. Height estimates were analyzed using polar-orbiting and geostationary satellite data, ground-based radar data, and reports from pilots (PIREPS) and ground observers. All these data were approximately concurrent in time for each eruption event.

Table 5.3. Examples of the variation in height estimates for the 2006 eruptions of Augustine Volcano. Generally, ground-based radar is considered more accurate and provides a discrete estimate compared with satellite techniques. Usually, satellite temperatures and trajectories are in general agreement and are often expressed as a range rather than a discrete value. However, during the recent Redoubt eruption some radar height estimates were often much higher (by a factor of 2) than those from other techniques.

Date	*Time* (UTC)	*BTD* (K)	*Plume T* (°C)	*Height estimate model* (km)				
				Radar	*Temperature*	*Trajectory*	*PIREP*	*Comments*
11-Jan-06	13:44	0		9		>8	—	
	13:48		−46		7–12			
	14:12	0	−45		7–12	9		
	14:25	0	−55		8.5		—	
13-Jan-06	13:24	0		10.5				
	13:28	0	< −54					Supercooled
	13:56	0	−52.5		8			
	17:47						14.5–16	
	19:24	0	−44		6.5			
	20:41	−1.4	−54	11	9.5		16	Ash on rim
	21:03	−4	−51.5	11	7.5			Ash on rim
14-Jan-06	01:45	−1.9	−55	10.5	8–8.5			Ash on rim
17-Jan-06	16:58			14				
	17:38	0	−55		8	8–9		

The eruption of Augustine Volcano on January 14, 2006 at 01:45 UTC is a good example of height estimates and how they may relate to the morphological structure of the plume (Figure 5.18). The volcano erupted at 01:40 UTC. Satellite data, radar, and an oblique photograph were recorded within minutes of each other. The photograph shows a central peak at a higher altitude (Figure 5.18a) surrounded by what appears to be a relatively flat plume at a lower altitude.

The satellite image shows a circular plume approximately 10 km across with a minimum temperature of −55°C for the central peak and −52°C for the surrounding plume top. The temperature of the central peak correlates to a height of about 8 km (Figure 5.18c) and, since the central peak temperature is not colder than the surrounding atmosphere, this shows that it is not supercooled. The temperature of the lower portion of the plume translates to atmospheric heights between 7.5 and 10 km while radar suggests a height of approximately 10 km. If height estimates were based solely on plume temperature a single definitive value could not be given but limits could be provided, such as greater than 7.5 km. One PIREP estimates the plume height to between 9 and 10.5 km which agrees with other estimates. The January 14 eruption is also a good example of how temperature is related to the structure of the plume. Comparing the photograph (Figure 5.18a) with the satellite image (Figure 5.18b) the thin edges of the plume (circles in the figure) have warmer temperatures (−25°C, blue) than regions closer to the center and, hence, are semi-transparent allowing background radiation to penetrate the cloud resulting in a warmer signal detected by the satellite sensors. In this example the semi-transparent edges are estimated to be less than 1 km thick based on comparing the dimensions of the plume width and plume height on satellite data with the perspective photography.

The structure of a volcanic cloud and its height are very dynamic, especially when the cloud is still attached to the volcanic vent. The dynamics are affected by variations in the heat and emissions from the volcano, structure of the atmosphere, entrainment of moisture, composition of the cloud (ash-rich, water-rich), presence of ice (Rose *et al.*, 1995), and the injection of aerosols. These conditions change in time as the cloud evolves (Tupper *et al.*, 2003, 2004, 2007). Moreover, these conditions impact the electromagnetic signal as a function of wavelength measured in satellite data, which might

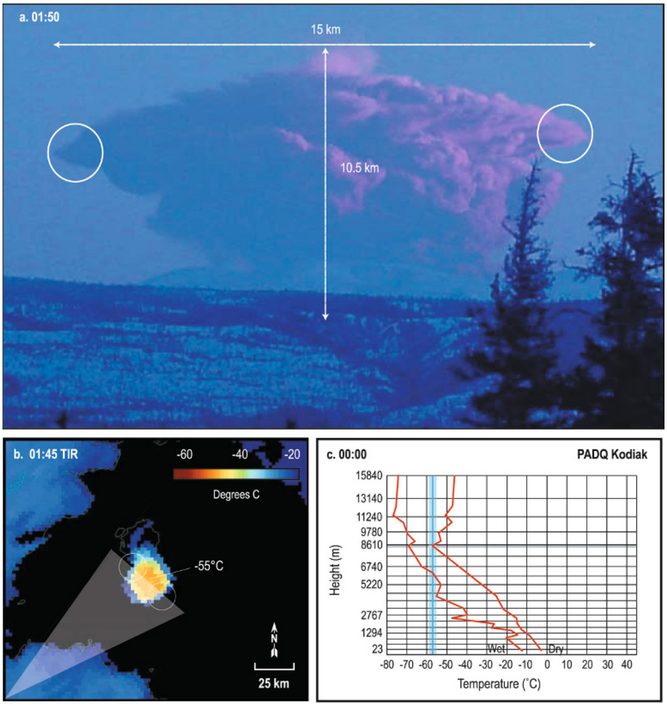

Figure 5.18. An oblique photograph of an eruption plume at Augustine taken on January 14, 2006, 01:50 UTC (a) shows a profile view of the plume recorded on a satellite image at 01:45 UTC (b). The satellite image shows the coldest part of the plume (yellow and orange) to be elliptical, 10 × 15 km in size, and 10.5 km high according to radar. The coldest temperature is −55°C near the center of the satellite image and decreases to −24°C (light blue) along the edges. Comparing the photograph with the satellite image shows that the thickest part of the plume coincides with the coldest regions (yellow and orange) and is presumably opaque. The warm edge of the plume (light blue) coincides with the thin edge in the photograph and is presumably semi-transparent as seen on the satellite image (open circles). The thin edge is estimated to be less than 1 km thick. The viewing direction of the photograph, the gray area in (b), is NE (modified from Bailey, 2010).

also help to explain some of the variations in height estimates.

A conceptual model of a plume (based on Turco *et al.*, 1983) shows gas and water vapor capping the plume with ash in the lower parts of the umbrella region of the plume (Figure 5.19). The boundary between the ash and gas-rich components is not an impenetrable barrier—but a transition. Pilots viewing the cloud are looking in the visible wavelengths and see Rayleigh scattering of light by gases at the very top of the cloud and, so, the viewing geometry greatly affects the accuracy of height estimates (Tupper *et al.*, 2003). Thermal infrared wavelengths used by satellite sensors record radiated energy that is emitted from a range of heights near the top of the cloud although it is assumed that most of the energy is radiated at the point where the plume is opaque (Sparks *et al.*, 1997). Therefore, the temperature measurement is an integrated value over a pixel area (spatial and depth) somewhere within the upper portion of the cloud. Thus, the cloud temperature and derived height is not solely from the cloud top. At radar wavelengths gas clouds are mostly transparent, but particles within clouds reflect microwave energy back to the sensor. The size of the particles detected by radar depends upon the wavelength used. The AVO and NEXRAD radars are sensitive to 1 to 0.01 mm size particles. Radar instruments detect particles that might be composed of ash or ice crystals or condensed droplets. Radar is probably more sensitive to fewer particles than satellite sensors.

From the perspective of satellite sensors alone one might expect height estimates from PIREPS to

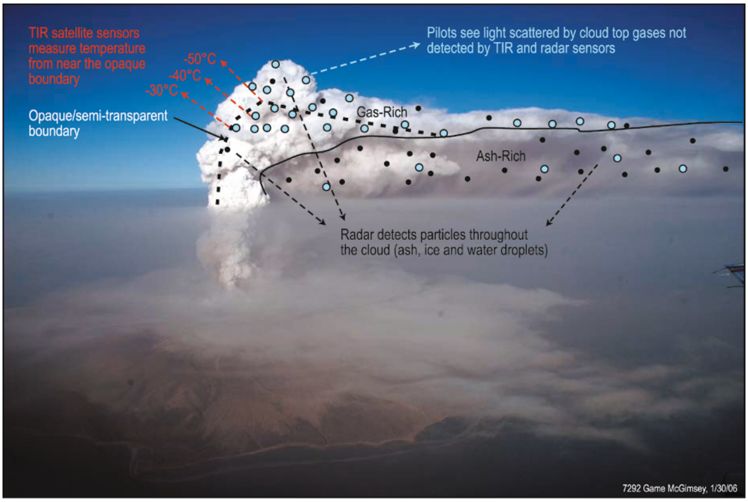

Figure 5.19. A conceptual model of a plume showing a gas-rich region capping the ash-rich region (modified from Lane *et al.*, 1995 and Turco, 1992). Pilots observe scattered light in the visible from volcanic aerosol layers (H_2SO_4, SO_2, and some ash). TIR satellite sensors detect radiated energy from multiple levels but near the opaque/semi-transparent boundary and measure an integrated temperature over a pixel but below the cloud top. Radar detects reflected energy from particles throughout the cloud as a function of its wavelength but gases are mostly transparent.

be higher than other methods (even if geometry was accounted for) and TIR satellite sensors somewhat lower than the visual cloud top due to cloud penetration. Radar data may provide a more accurate height estimate of ash particles but the signal may be from particles other than ash, be sensitive to particle concentrations below satellite detection limits, and will ignore gas components. The height of a plume, particularly during its initial stages, changes rapidly (on the order of minutes) and the timing of observations is critical for these estimates. Even if the observations are coincident in time they are affected by different conditions, so plume height estimates will vary between techniques.

5.9 PHYSICAL PRINCIPLES OF ASH DETECTION IN THE INFRARED

5.9.1 Volcanic ash detection

Volcanic ash is a hazard to aircraft and, therefore, needs to be detected and its movement tracked (Casadevall, 1994; Casadevall *et al.*, 1996; Miller and Casadevall, 1999). The problem of detecting volcanic clouds using satellite data is really a problem of discrimination. Ash clouds absorb, emit, and scatter radiation in the visible, infrared, and microwave regions of the electromagnetic spectrum. At visible wavelengths, depending on the geometry of illumination (by the Sun or using a laser light source) and the geometry of observation, clouds may appear bright or dark. This is true of clouds of water, ice, silicates (volcanic ash), wind-blown dust (desert dust), smoke (e.g., from a large forest fire) or any other naturally or anthropogenically generated cloud of particles. It is sometimes very clear that a particular cloud is meteorological in origin (e.g., a cloud of water droplets or ice particles, or a mixed phase cloud), but often not so clear that it is not a meteorological cloud. Figure 5.20a–h shows some satellite images of anomalous clouds in the atmosphere. These are daytime MODIS images that have been enhanced to provide a true-color rendition of the scene. In all of these scenes there are meteorological clouds and clouds due to other sources: (a) a thick ash column rising above Ruang Volcano (Sangihie Islands, Indonesia, 125.37°E, 2.30°N), (b) a drifting ash and gas plume recently emitted from Karthala Volcano (Comoros, 11.75°S, 43.38°E), (c) a low-level gas (predominantly SO_2 and H_2O) plume from Ambrym Volcano (Vanuatu, 16.25°S, 168.12°E), (d) an ash and gas plume over snow-covered terrain from

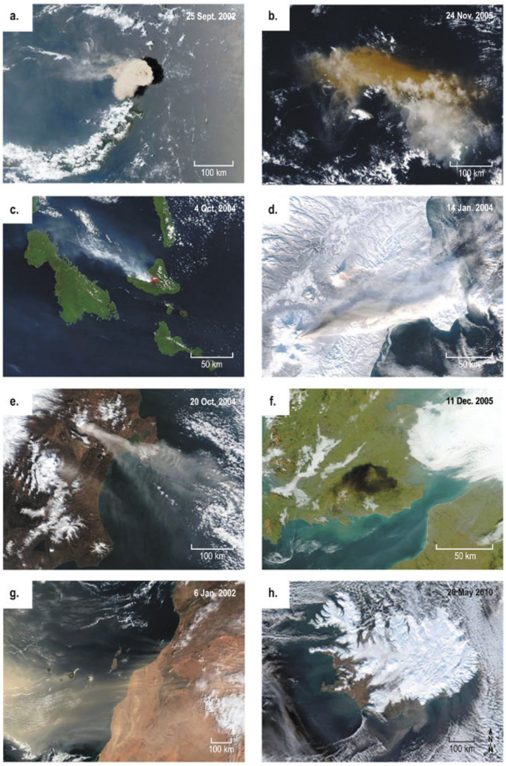

Figure 5.20. Daytime MODIS scenes showing anomalous clouds: (a) thick ash column from Ruang Volcano; (b) drifting ash and gas plumes from Karthala Volcano; (c) low-level gas cloud plume from Ambrym Volcano; (d) ash and gas plume over snow-covered terrain (Kliuchevskoi Volcano); (e) ash and gas plume from Shiveluch Volcano; (f) a noxious gas cloud from an industrial fire in southern England; (g) a dust outbreak over the Canary Islands; and (h) surface ash re-suspended by wind streaming off the southern coast of Iceland (images are courtesy of NASA Earth Observatory website).

Kliuchevskoi Volcano (Kamchatka, 56.057°N, 160.638°E) , (e) an ash and gas plume from Shiveluch but in summer, (f) a noxious cloud generated from an industrial accident in southern England, (g) a dust outbreak traveling westwards over the Canary Islands (28.00°N, 15.58°W), and (h) wind-blown ash off the coast of Iceland. These examples illustrate some of the variability found in anomalous clouds when viewed by satellites during the day. Some clouds appear almost black (Figure 5.20f) or dark gray (Figure 5.20h), some are as white as water/ice clouds (Figure 5.20c, d), while others take various sandy shades with brown and yellow hues (Figure 5.20a, b, e, g). By using objective analysis of daytime visible imagery alone, it has been very difficult to unambiguously discriminate ash clouds from other clouds. During the nighttime, the task is made even more difficult because there is no sunlight available and, hence, the visible satellite channels cannot be used. This is the main reason researchers have turned their attention to using infrared data (e.g., Hanstrum and Watson, 1983; Prata, 1989a, b; Barton *et al.*, 1992; Ellrod *et al.*, 2003).

5.9.2 Transmission of EM energy through a cloud

Satellite-borne infrared radiometers are used to measure atmospheric radiation in narrow (0.5–1.0 μm) wavelength bands, collecting energy from all components of the scene within the field of view of the instrument. In general terms, it is possible to write down the radiative transfer equation (RTE) governing this kind of measurement, with some suitable approximations to make the problem tractable. A useful starting point is to consider a directional (downwards) measurement of the upwelling radiation from a cloud-less atmosphere over a narrow band of infrared wavelengths, where the contributions from solar radiation are negligible, ignore infrared scattering, and adopt plane-parallel geometry. With these conditions, we may write:

$$I_\lambda(\varphi,\theta) = I_{s,\lambda}(\varphi,\theta)\tau_{s,\lambda}(\varphi,\theta) + \int_0^\infty B_\lambda[T(z)]\frac{\partial \tau_\lambda(z;\varphi,\theta)}{\partial z}dz \qquad (5.2)$$

where I is the directional radiance measured at the sensor; I_s is the radiation from the surface; B is the Planck function; T is temperature; $T(z)$ is the vertical temperature profile; λ is wavelength; z is height; τ is the atmospheric transmittance; φ is the azimuth angle; and θ is the zenith angle.

All quantities are to be considered as averages over a narrow band; for notational convenience the band is designated by a single wavelength that represents the band-averaged central wavelength. The radiance measured consists of two terms: the first term represents radiation from the surface and the second term represents radiation (emission and absorption) from the atmosphere. The surface term can be divided further into surface emission and radiation from the atmosphere reflected back off the surface:

$$I_{s,\lambda} = \varepsilon_{s,\lambda}(\varphi, \theta) B_\lambda[T_s] + \frac{1}{2\pi} \int_\Omega I_{a,\lambda}(\varphi, \theta) \rho_{s,\lambda}(\varphi, \theta) \cos\theta \sin\theta \, d\Omega \quad (5.3)$$

where W is the solid angle; $\varepsilon_{s,\lambda}$ is the surface emissivity; ρ is the bi-directional reflectance distribution function; and T_s is the surface temperature. An assumption often made, and one that will be made here, is to take:

$$\varepsilon_{s,\lambda} = 1 - \rho_{s,\lambda} \quad (5.4)$$

which assumes that the surface is Lambertian (i.e., there is no preferred direction for reflected radiation). Let us now introduce a plane-parallel cloud into this plane-parallel model[1] and adjust the RTE to include this layer:

$$I = I_s + I_a + I_c + I_\uparrow \quad (5.5)$$

where I_a is the atmospheric radiance but with the upper limit of the integral terminated at the base of the cloud (z_b); and I_c is the cloud radiance. We have omitted the notation for wavenumber and angular dependence for convenience. The term $I_\uparrow$ represents atmospheric radiation above the cloud top (z_t) and can often be ignored for window channels and when the cloud is high. There is also radiation from above the cloud that is reflected off the cloud back towards the sensor, but this is a very small contribution and can be safely neglected. An idealized depiction of the model is shown in Figure 5.21. While scattering has been ignored in the atmosphere, it cannot be ignored in the cloud. In fact, without including the effects of scattering, the foundations for detecting ash clouds using infrared instruments would be flawed. The RTE for scattering by a layer of particles can be written:

$$\mu \frac{\partial I}{\partial t}(t, \mu) = I(t, \mu) - (1 - \varpi_0) B(T) - \frac{\varpi_0}{2} \int_{-1}^{1} P(\mu; \mu') I(\tau, \mu') \, d\mu' \quad (5.6)$$

where $t = -\ln(\tau)$ is the optical depth; μ is the cosine of the zenith angle; ϖ_0 is the single-scattering albedo; and P is the axially symmetric phase function. The cloud layer has an optical depth t_1 and we are only concerned with the upwelling radiance in the direction μ at the cloud top ($\tau = 0$). This equation can be solved using boundary conditions of no downward radiance incident on the cloud top:

$$I(0, -\mu) = 0 \quad (5.7)$$

and the upward radiance incident on the cloud base is due only to that emitted from the ground:

$$I(t_1, +\mu) = I_v \quad (5.8)$$

The plus and minus signs signify upward and downward directions, respectively. Thus, to model radiative transfer it is necessary to calculate (or measure) the radiance emitted by the surface and atmosphere beneath the cloud and be able to characterize the optical properties of the scatterers inside the cloud as a function of wavelength. Given that the RTE described above is quite complex it is informative to use a highly simplified model that still captures the important features of infrared sensing of volcanic ash clouds. Such a model is described next and we will return to the more complex treatment in Section 5.10.2.

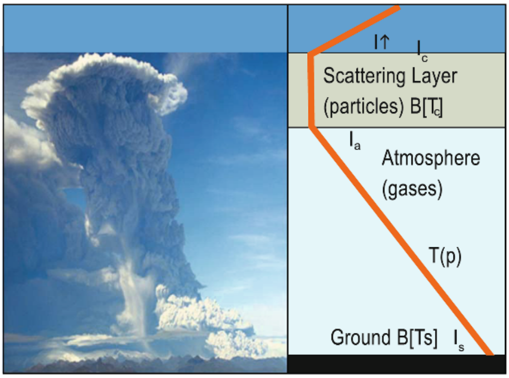

Figure 5.21. Idealized radiative transfer model for calculating radiation propagation through an absorbing atmosphere and scattering layer of cloud particles (see text for the meaning of the various terms).

5.10 MODELING RADIATIVE TRANSFER IN ASH CLOUDS

5.10.1 A simplified model

In order to isolate the important factors affecting the RT inside an ash cloud, some simplifying assumptions are made. First, the atmosphere below the cloud layer is assumed to be totally transparent:

---

[1] The assumption of plane-parallel conditions is not particularly limiting, but simplifies the mathematical treatment. These equations can be re-cast for a spherical shell atmosphere and an arbitrarily shaped cloud.

$I_a = 0$. Second, the Earth's surface below the cloud is assumed to be a blackbody: $I_s = B[T_s]$. Third, we consider nadir viewing only: $\varphi = 0, \theta = 0$. Fourth, we consider the cloud to consist of homogeneous particles at a single temperature, T_c. Finally, rather than consider a broad spectrum of narrow bands, we take just two:

$$I_{\lambda_1} = B_{\lambda_1}[T_s]\exp(-t_1) + (1-\exp(-t_1))B_{\lambda_1}[T_c] \quad (5.9)$$

$$I_{\lambda_2} = B_{\lambda_2}[T_s]\exp(-t_2) + (1-\exp(-t_2))B_{\lambda_2}[T_c] \quad (5.10)$$

These two equations can be linearized (see Prata and Grant, 2001 for details) and, noting that the cloud emissivity is $1 - \exp(-t)$, we may write:

$$T_1 = T_s(1 - \varepsilon_1) + \varepsilon_1 T_c \quad (5.11)$$

$$T_2 = T_s(1 - \varepsilon_2) + \varepsilon_2 T_c \quad (5.12)$$

$$\varepsilon_i = 1 - \exp(-t_i) \quad (5.13)$$

$$t_i = k_i L \quad (5.14)$$

where k_i is the absorption coefficient of the particles at wavelength i; and L is the geometric thickness of the cloud. These equations can be solved to obtain:

$$\Delta T = \Delta T_c(X - X^{\beta}) \quad (5.15)$$

$$X = 1 - \frac{\Delta T_1}{\Delta T_2} \quad (5.16)$$

$$\beta = \frac{k_1}{k_2} \quad (5.17)$$

where $\Delta T = T_1 - T_2$; $\Delta T_c = T_s - T_c$; and $\Delta T_1 = T_s - T_1$. The important physics is captured in the parameter β, which represents the ratio of extinction coefficients at two wavelengths, λ_1 and λ_2. It is possible to explore the parameter range of β, guided by typical values for the extinction coefficients. Since the two wavelengths are usually close together the extinction coefficients are not very different and $\beta \approx 1$.

Figure 5.22 shows the variation of ΔT with T_1 for $\beta < 1$, $\beta > 1$, and $\beta = 1$. When $\beta < 1$, the extinction coefficient at $k_{\lambda_1} > k_{\lambda_2}$ leads to a U-shaped curve, while for the opposite case $\beta > 1$ an arch-shaped curve results. If $\beta = 1$ then ΔT has no variation with T_1 and no information can be retrieved from this analysis. It turns out that for $\lambda_1 \approx 11\ \mu\text{m}$ and $\lambda_2 \approx 12\ \mu\text{m}$, typical of channels on many satellite sensors, $\beta < 1$ for silicates (ash particles) and $\beta > 1$ for water molecules and ice particles. If one were free to design a sensor solely for ash detection, it would be sensible to select channels that optimize the U-shaped curve.

One of the main problems with identifying ash in a cloud arises because often the ash is in a mixture with liquid water droplets or ice particles. Liquid water and ice clouds have $\beta > 1$ and therefore cause an opposite effect to that brought about by ash clouds on the ΔT vs. T_1 diagram. The simple model can be examined further to correct for water vapor effects, or at least understand how these effects manifest themselves. Assuming that the temperature difference observed arises from a linear combination of the signal from ash (ΔT_{ash}) and the signal due to water vapor (ΔT_{wv}), a two-component model can be developed. If the fraction of ash in the mixture is F, then we may write the observed temperature difference as:

$$\Delta T = F \Delta T_s [Z - Z^{\beta}] \quad (5.18)$$

where

$$Z = 1 - \frac{1}{F}\frac{\Delta T_1}{\Delta T_s} \quad (5.19)$$

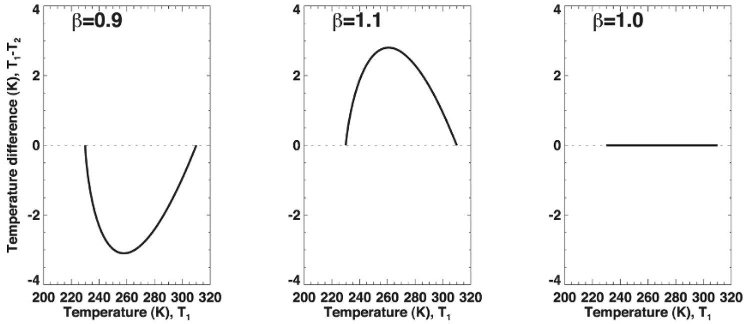

Figure 5.22. Variation of $rT = T_1 - T_2$ with T_1 for three values of the parameter β. When $\beta = 0.9$ (left panel) a characteristic U-shaped curve is found, indicative of silicate particles. Conversely, when $\beta = 1.1$ (middle panel) the curve is arch-shaped and indicates liquid water droplets or ice particles. When $\beta = 1$, there is no variation with T_1.

The other parameters are defined as before. Ideally, this procedure needs to be automated. There are several parameters that can be determined from the image data. These are:

(1) the clear sky surface temperature T_s;
(2) the cloud top temperature T_c;
(3) the clear sky value of the water vapor correction; and
(4) the ratio of extinction coefficients β that governs the magnitude of the U-shaped distribution of negative differences.

A procedure for estimating these parameters from image data has been developed. A brief outline is given below:

1. T_s—this is easily estimated by finding the maximum value of T_1 occurring in the data. If the scene is too cloudy then an estimate from a climatology or from analysis data can be used.
2. T_c—this is more difficult to estimate from the data, because the lowest value may not necessarily correspond to the volcanic cloud. However, provided an area in close proximity to the suspect cloud can be delineated it may be reasonable to assume that the lowest value is the cloud top temperature. As the cloud top height can vary the use of a single T_c may introduce errors.
3. *Water vapor correction*—an empirical relation (Yu *et al.*, 2002) between the precipitable water in an atmospheric column and the brightness temperature difference $(T_1 - T_2)$ is used to estimate the water vapor effect:

   $$\Delta T_{\text{wv}} = \exp[6T_* - b] \qquad (5.20)$$

   where $T_* = T_1/T_{\max}$; and $T_{\max}$ is an arbitrary normalization constant assigned a value of 320 K. The free parameter b essentially determines the value of the water vapor effect on $T_1 - T_2$ at the maximum value of T_1. Hence, b can be determined directly from the image data, allowing realistic flexibility on the size of the water vapor correction determined by this semi-empirical approach. Values of b between 3 to 5 appear to be acceptable.
4. b—theoretical estimates of β suggest a value of around 0.7. A method for estimating β, T_s, and T_c simultaneously has been developed by using the distribution of T_1 vs. $T_1 - T_2$. The distribution is first histogrammed (or binned) into intervals of 0.5 K in T_1. Then, the lowest values in each bin are found and a curve is generated giving the outline of the distribution. The curve is smoothed and fitted using a nonlinear least squares model. The model has three parameters—T_s, $T_s - T_c$, and β—that can be estimated from the fit.

The curve-fitting procedure uses the model developed earlier with $F = 1$ and the partial derivatives of the model, which are analytic. Writing:

$$Y = \alpha(X - X^\beta) \qquad (5.21)$$

where $Y = T_1 - T_2$, $\alpha = T_s - T_c$, $X = 1 - (\gamma/\alpha)$, $\gamma = T_s - T_1$. The partial derivatives are:

$$\frac{\partial Y}{\partial \alpha} = (X - X^\beta) + \frac{\gamma}{\alpha} + \beta\frac{\gamma}{\alpha}\left(1 - \frac{\gamma}{\alpha}\right)^{\beta-1} \qquad 5.22)$$

$$\frac{\partial Y}{\partial \beta} = \alpha X^\beta \log \beta \qquad (5.23)$$

$$\frac{\partial Y}{\partial \gamma} = 1 - \beta X^{\beta-1} \qquad (5.24)$$

An example of the correction procedure is shown in Figure 5.23. The characteristic U-shaped curve indicating ash is apparent in the uncorrected (black dots) and water vapor corrected (red dots) data. The solid line is determined from the simple model using a suitable value of β and values for T_s and T_c. The important point to note is that the water vapor correction does not simply decrease all the values uniformly, rather the correction rotates the points in a clockwise direction about a point close to $\Delta T = 0$ and $T_{11\,\mu\text{m}} = T_s$. This gives larger correction to points closer to T_s; points that are nearer the surface and hence expected to be affected greater by water vapor. The simple model considers only absorption as the process for extinction of IR radiation. In reality, scattering is also important and, unfortunately, this requires more complex modeling and the use of numerical methods.

5.10.2 Complex RT model

Prata (1989a, b), Wen and Rose (1994), Prata and Grant (2001), and Watson *et al.* (2004) have proposed RT models to solve the IR absorption/scattering processes for a volcanic ash cloud. The models essentially follow the theory outlined above, but the methods of solution differ in detail.

Wen and Rose (1994) and Prata and Grant (2001) have shown that, by including a microphysical model of the ash particles with a detailed

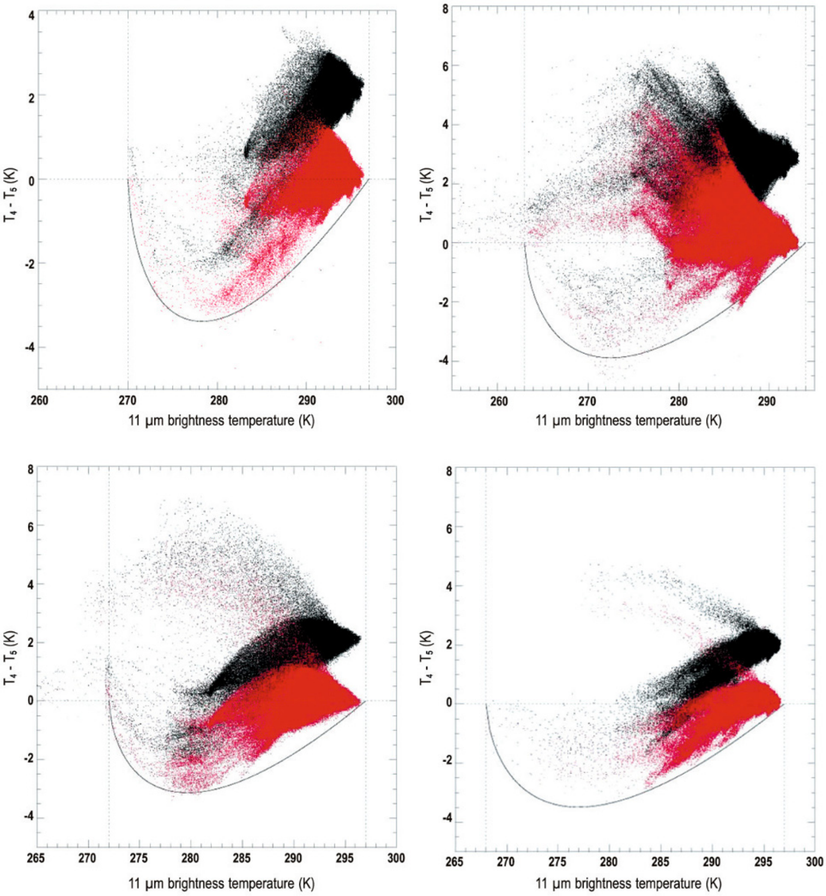

Figure 5.23. Temperature difference distributions without water vapor corrections (black dots) and with corrections (red dots). The water to vapor correction was applied to four different volcanic clouds using AVHRR data. T_4 and T_5 are AVHRR channel 4 (11 μm) and 5 (12 μm) brightness temperatures that correspond to T_1 and T_2 used in the theory here.

radiative transfer model, infrared data can be inverted to reveal mean particle size and cloud opacity. When these parameters are integrated over the area covered by the cloud, the total mass and mass loading can be inferred from the data. These are quantifiable products that may be incorporated in dispersion models to generate risk maps for use by the aviation industry. An example of this kind of retrieval is given in Figure 5.24 for the Karthala eruption.

There are many satellites (polar and geosynchronous) that carry these infrared channels, so this product can be delivered globally. Table 5.4 gives details of some of the satellite instruments capable of providing ash mass loadings.

5.10.3 Retrieval method

The radiative transfer required to extract quantitative information from infrared window radiances (8–12 μm) employs Mie theory and plane-parallel radiative transfer in an absorbing and scattering cloud. Given the real and imaginary parts of the index of refraction of the ash cloud particle as a function of wavelength, as well as the particle shape and size distribution, then the efficiencies for scattering, absorption, and extinction can be calculated using a Mie scattering program. There is scant information on particle shapes in real ash clouds and only approximate methods exist for calculating efficiencies for particles of arbitrary shapes. We

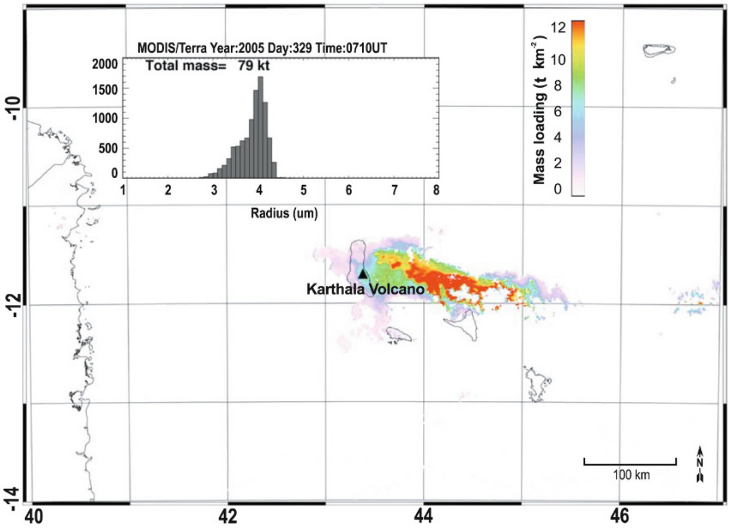

Figure 5.24. MODIS ash mass concentrations in t km^{-2} (or g m^{-2}) for an eruption of Karthala Volcano, November 2005.

Table 5.4. Details of past and current satellite instruments that can be used to detect ash and generate ash mass loading maps from infrared measurements.

Satellite	*Instrument*	*Spatial resolution* (km × km)	*Temporal resolution* (per day)	*Time period covered*
NOAA	AVHRR-2, -3	1 × 1	2	1981–present
NOAA	HIRS-2, -3, -4	10 × 10[a]	2	1979–present
GOES	VISSR/VAS	5 × 5	24	1980–present
ENVISAT	ATSR family	1 × 1	2[b]	1991–present
GMS-5	VISSR	5 × 5	24	1995–present
Terra/Aqua	MODIS	1 × 1	4[c]	1999–present
Aqua	AIRS	14 × 14	2	2002–present
MetOp	IASI	12 × 12	2	2007–present
MSG	SEVIRI	3 × 3	96	2006–present

[a] Earlier HIRS (1–3) instruments had a larger field of view of 18 × 18 km^2.
[b] These satellites are in a 3-day repeat cycle such that the same point imaged twice in one day will not be imaged again until 3 days later.
[c] Assuming two satellites in orbit at any given time.

assume that the particles are spherical and the exact Mie theory computer program of Evans (1988) is employed to calculate the efficiencies. Some measurements exist for the particle size distribution at the edges of the Mt. St. Helens ash cloud (see the papers in Newell and Deepak, 1982). These data indicate that a log-normal (or ZOLD) size distribution gives a reasonable fit to the distribution. The measurements reported by King *et al.* (1984) and Hofmann and Rosen (1984) of the El Chichón stratospheric aerosol layer (King *et al.*, 1984; Matson, 1984) fit a modified-γ size distribution quite well. These data generally pertain to volcanic aerosol layers that are relatively old and high in the atmosphere. Only the fine particles can be detected in nascent and low (tropospheric) volcanic plumes, and it is assumed that the size distributions would be similar to those reported for El Chichón (Hofmann and Rosen, 1984) and Mt. St. Helens. Both size distributions have been used to perform radiative transfer calculations and, although there were differences in detail between the results for the two distributions (see also Wen and Rose, 1994), the basic results and mass loadings were essentially the same.

The parameters used in the Mie program are described in Prata (1989b). Once the Mie program has been run for each value of the size parameter (mean particle size and monochromatic wavelength), scattering parameters are then fed into a plane-parallel discrete ordinates radiative transfer program (Stamnes and Swanson, 1981). Given the single-scattering albedo, asymmetry parameter, extinction and scattering efficiencies as a function of monochromatic wavelength, and the cloud top and surface temperatures, radiances emerging from the top of the cloud along n distinct streams (zenith angles) can be computed. These radiances are calculated for cloud optical depths ranging from 0 to 20 at wavelengths corresponding to the thermal IR channels of the sensor (e.g., AVHRR, MODIS, SEVIRI, etc.) for atmospheres that contain no water. On completion of these calculations, a large two-dimensional (corresponding to the 11 and 12 μm channels) look-up table exists with entries at prescribed values of the mean particle size r_m and optical depth τ. Each entry in the table consists of pairs of brightness temperatures $T_{11\,\mu\text{m}}$ and $T_{12\,\mu\text{m}}$. The retrieval then consists of locating the (r_m, τ) pairs within the look-up table that best match ($T_{11\,\mu\text{m}}$, $T_{12\,\mu\text{m}}$) measurements at each image pixel.

The calculations were performed assuming that there is no absorption of infrared radiation by water vapor. The effects of atmospheric water vapor absorption on satellite brightness temperatures can be assessed by performing radiative transfer calculations. The radiative transfer model Modtran 3 (Berk *et al.*, 1989) was used to calculate the temperature difference between satellite-measured brightness temperatures at the 11 and 12 μm wavelengths, at each vertical level using the temperature and moisture structure from a nearby radiosonde profile. The results of this analysis show that the effect of water vapor is greatest at the lowest levels, where it typically exceeds 1 K. At higher levels, near the location of the plume, the effect is less than 0.2 K. In the tropics and under high-humidity conditions, the effect of water vapor absorption can mask out the "reverse" absorption effect of volcanic ash clouds. This can lead to misidentification of volcanic clouds and is a limitation of the current thermal detection method.

5.10.4 Size distributions, scattering parameters, and mass loading

The modified-γ distribution has the functional form:

$$n(r) = N_0 \frac{r^{\alpha}}{\Gamma\left[\dfrac{\alpha+1}{\gamma}\right]} b^{(\alpha+1)/\gamma} \exp(-br^{\gamma}) \qquad (5.25)$$

where $n(r)$ is the number of particles per unit volume; r is the particle radius; Γ is the Gamma function (see Press *et al.*, 1986, p. 156); N_0, b, α, and γ are parameters of the distribution. The size parameter x is related to the particle radius and the wavelength λ through:

$$x = \frac{2\pi r}{\lambda} \qquad (5.26)$$

where $\gamma = 1$; $\alpha = 6$; $b = 6/r_0$. Equation (5.25) reduces to:

$$n(x) = Cx^6 \exp\left(-\frac{6x}{x_0}\right) \qquad (5.27)$$

where C is a constant replacing the other parameters. Within a distribution of sizes, the mode radius r_0 corresponds to the mode size parameter x_0.

The log-normal distribution is described by:

$$n(x) = N_0 \frac{1}{\sigma_x} \exp\left[-\frac{(Ln(x) - Ln(x_0))^2}{2\sigma_x^2}\right] \qquad (5.28)$$

where, as before, x is the size parameter. The parameter $\sigma_x = 2\pi\sigma_r/l$ is related to the standard deviation (σ_r) of the distribution and is a measure of its spread. In the calculations performed with this distribution, σ_r was set to 0.5, 0.75, 1.0, and 1.25 μm and results were reported for $\sigma_r = 1.0$ μm.

The inputs to the Mie program are the real and imaginary parts of the refractive index (m), the size parameter, and the size distribution. The outputs are the extinction efficiency ($\hat{Q}_{\text{EXT}}$), scattering efficiency ($\hat{Q}_{\text{SCA}}$), and phase function ($P(\theta)$). For polydispersions these efficiency factors are related to the single-particle efficiencies ($\hat{Q}_f$) by:

$$\hat{Q}_f = \frac{\int_0^\infty \pi r^2 Q_f\left(\frac{2\pi r}{\lambda}, m\right) \frac{dn(r)}{dr} dr}{\int_0^\infty \pi r^2 \frac{dn(r)}{dr} dr} \tag{5.29}$$

The absorption efficiency is then:

$$\hat{Q}_{\mathrm{ABS}} = \hat{Q}_{\mathrm{EXT}} - \hat{Q}_{\mathrm{SCA}} \tag{5.30}$$

The remaining parameters needed to perform radiative transfer calculations which relate to the cloud microphysical structure are the single-scattering albedo:

$$\varpi = \frac{\hat{Q}_{\mathrm{EXT}}}{\hat{Q}_{\mathrm{SCA}}} \tag{5.31}$$

and the asymmetry parameter:

$$g = \frac{1}{2}\int_{-1}^{1} P(\theta)\cos\theta d\cos\theta \tag{5.32}$$

where θ is the scattering angle. The number of particles per unit volume in the cloud is:

$$N = \int_0^\infty \frac{dn}{dr} dr \tag{5.33}$$

The optical depth of the cloud is:

$$\tau_\lambda = \pi L \int_0^\infty r^2 Q_{\mathrm{EXT}}(r, \lambda) n(r)\, dr \tag{5.34}$$

where L is the geometrical thickness of the cloud. The mass loading (kg m^{-2}, mg mm^{-2} or kt km^{-2})[2] is

$$M = \tfrac{4}{3}\pi\rho L \int_0^\infty r^3 n(r)\, dr \tag{5.35}$$

where ρ is the density of the ash.

5.10.5 Mass loadings

The U.S. Military consider mass concentrations $>50\,\mathrm{mg\,m^{-3}}$ a potential hazard to their aircraft operations. Przedpelski and Casadevall (1994) estimated a mass concentration of $\approx 2{,}000\,\mathrm{mg\,m^{-3}}$ at 25,000 ft ($\approx$7.5 km) for the December 15, 1989 Redoubt eruption cloud that caused significant damage to a KLM Boeing 747-400 jet aircraft. Mass loadings include all particles with radii $<50\,\mu$m which have atmospheric residence times of the order of at least a few hours. Having determined the particle size distribution, the geometrical thickness of the cloud, and its areal extent, it is possible to estimate the mass loading of fine particles in an ash plume. The density of the ash is taken to be 2,600 kg m^{-3} and the area of a pixel is typically taken as $\sim$1 km^2—this is a mean area for pixels for both the AVHRR-2 and MODIS; pixels near the scan edges will be somewhat larger (several km^2). Pixels are counted if they satisfy the criterion $DT < T_{\mathrm{cut}}$, where T_{cut} is a threshold usually taken as 0 K and the retrieved particle size is in the range $1 < r_m < 8\,\mu$m. An estimate of the cloud thickness is crucial to the evaluation of mass concentrations. Data on cloud thicknesses are not available so they must be estimated by other means. Studies of plume rise in stable stratified atmospheres (e.g., Briggs, 1975) suggest that, to a reasonable approximation, the vertical extent of a plume can be estimated from the cloud top height. For example, Manins (1985) has calculated the heights and vertical extents of stabilized smoke plumes as a function of power release and, following Briggs (1975), suggests that the vertical extent (cloud thickness) Δz of these plumes is given by:

$$\Delta z = 0.4 z_{\mathrm{top}} \tag{5.36}$$

where z_{top} is the height of the plume top. New measurements from the CALIOP lidar (Winker *et al.*, 2007) on board CALIPSO suggest that drifting volcanic plumes are no more than 1–3 km thick, but variable. The variability of cloud thickness along the plumes and the problem of not having simultaneous plume top height and plume base height data for each of the plumes means that we cannot estimate plume thickness to any greater accuracy. The total mass can be calculated by multiplying (5.36) by the area of a pixel.

5.10.6 Retrieval procedure

In the ($T_{11\,\mu\mathrm{m}}$, $T_{11\,\mu\mathrm{m}}$–$T_{12\,\mu\mathrm{m}}$) plane there exist isolines of constant mean particle radius r_m^j. Each point on the isoline r_m^j corresponds to particular values of the optical depth $\tau^{j,i}$. Lines connecting equal values of $\tau^{j,i}$ also exist. Given the measured values ($T^*_{11\,\mu\mathrm{m}}$, $T^*_{12\,\mu\mathrm{m}}$), the retrieval procedure requires us to find the best values of (τ, r_m). Linear interpolation is adopted:

- Find values of $T_{11\,\mu\mathrm{m}}(\tau^{j,i}, r_m^j)$ that bracket $T^*_{11\,\mu\mathrm{m}}$. Label these:

  $$T^1_{11\,\mu\mathrm{m}}(r^j_m), T^2_{11\,\mu\mathrm{m}}(r^j_m) T^1_{11\,\mu\mathrm{m}}(r^{j+1}_m) T^2_{11\,\mu\mathrm{m}}(r^{j+1}_m)$$

- Interpolate on the r_m^j isolines to find the appropriate $\Delta T(r_m^j) = T_{11\,\mu\mathrm{m}}(r_m^j) - T_{12\,\mu\mathrm{m}}(r_m^j)$:

---

[2] 1 mg mm^{-2}= 1 kt km^{-2}.

$$\Delta T(r_m^j) = w_1 \Delta T_2(r_m^j) + (1 - w_1)\Delta T_1(r_m^j) \quad (5.37)$$

$$w_1 = \frac{T^1_{11\,\mu\mathrm{m}}(r_m^j) - T^*_{11\,\mu\mathrm{m}}}{T^1_{11\,\mu\mathrm{m}}(r_m^j) - T^2_{11\,\mu\mathrm{m}}(r_m^j)} \quad (5.38)$$

Similarly for $\Delta T(r_m^{j+1})$:

$$\Delta T(r_m^{j+1}) = w_2 \Delta T_2(r_m^{j+1}) + (1 - w_2)\Delta T_1(r_m^{j+1}) \quad (5.39)$$

and the weight w_2 is defined in an analogous way to w_1.

- The required mean particle radius is obtained using linear interpolation:

$$r_m^* = w_r r_m^j + (1 - w_r) r_m^{j+1} \quad (5.40)$$

$$w_r = \frac{\Delta T(r_m^{j+1}) - \Delta T^*}{\Delta T(r_m^{j+1}) - \Delta T(r_m^j)} \quad (5.41)$$

- In practice there are n isolines of r_m^j ($j = 1, n$), n is small ($n = 18$), and there are many more values of $\tau^{j,I}$ ($i = 1, k$) ($k = 100$ is used in the current software). Thus, $2n \times k$ values of ΔT are precomputed.

In summary the solution process for determining mass loadings from two-channel IR sensors entails:

- specifying the cloud geometry;
- specifying the viewing geometry;
- determining boundary conditions at the cloud;
- specifying the refractive indices of ash as a function of wavelength;
- specifying the size distribution and particle shape; and
- solving for cloud optical depth, particle size (radius), and mass using multi-scattering radiative transfer code.

Studies (e.g., Wen and Rose, 1994) have shown that the calculation is sensitive to the size distribution, particle shape, and refractive indices used, and errors as large as 40% can arise from inaccurate knowledge of these parameters.

5.11 MICROPHYSICAL VOLCANIC CLOUD MODEL

The new (e.g., MODIS) and proposed advanced multispectral sensors (e.g., GLI, SEVIRI, AIRS, IASI) include many channels capable of providing detection and discrimination of volcanic ash clouds. A model of an ash cloud has been developed in order to exploit these new sensors. We include information from the visible to infrared—although most of the discussion has centered on infrared window radiances, it seems likely that visible and near-infrared data may also provide a means for ash cloud detection.

At near-infrared wavelengths ($\lambda = 1.61$ µm, for example) ice clouds appear much darker than clouds of water droplets, because the imaginary part of the refractive index of ice is larger than that of water at this wavelength and, consequently, ice absorbs more strongly at this wavelength. A comparison of the refractive indices of water, ice, and andesite (a common constituent of ash clouds) is given in Table 5.5.

Pollack *et al.* (1973) list refractive indices of andesite (and some other minerals) over a large range of wavelengths from the UV to the infrared.

Table 5.5. Refractive indices for water, ice, and andesite (a silica-rich volcanic rock). The last column gives the reference to the origin of the data shown.

Wavelength (µm)	n_r	n_i	*Reference*
Ice			
0.63	1.309	1.04×10^{-8}	Masuda and Takashima (1990)
1.61	1.289	3.41×10^{-4}	Masuda and Takashima (1990)
Water			
0.63	1.332	1.44×10^{-8}	Masuda and Takashima (1990)
1.61	1.317	0.87×10^{-4}	Masuda and Takashima (1990)
Andesite			
0.68	1.470	1.70×10^{-3}	Pollack *et al.* (1973)
1.61	1.470	3.30×10^{-3}	Pollack *et al.* (1973)

These data are not the only source of refractive index values for minerals (see, for example, Ivlev and Popova, 1973; Volz, 1973; Sokolik and Toon, 1999). We have used the Pollack *et al.* values as a starting point to provide the input optical parameters required for more detailed radiative transfer calculations, and we propose a model of a volcanic ash cloud based on the Pollack *et al.* refractive indices of andesite. The ash cloud model consists of spherical andesite particles in a log-normal size distribution with a mean particle radius of 3 μm. The single-scattering albedo, asymmetry parameter, as well as the coefficients of absorption, scattering, and extinction are calculated for the polydisperse particle size distribution using the Mie program discussed earlier. Prata and Grant (2001) provides a listing of the the variation of single-scattering albedo (ϖ), extinction coefficient (Q_{EXT}), and asymmetry parameter (g) for wavelengths ranging from 0.3 to 14.5 μm—the range most commonly used in remote sensing of the Earth's atmosphere. Also shown are the results for a model ash cloud with mean particle radii of 1 and 5 μm.

5.11.1 Volcanic ash products

The main operational use for volcanic ash detection and retrieval is to assist aviation in the avoidance of hazardous ash clouds. The research and development for these algorithms has taken place at many different universities and research agencies and transferred for use at Volcanic Ash Advisory Centers (VAACs). There are nine VAACs (see Table 5.6) that cover almost all of the global flight regions, and these are sited at national meteorological centers and tend to utilize local R&D. This has led to a diversity of ash detection schemes and products, but nearly all are based on the reverse absorption method or an improvement to it. Some schemes utilize the 3.7 μm channel (see Table 5.7), and VAACs that rely on geosynchronous data tend to use single-channel visible and/or infrared temporal information. Several of the VAACs have posted case studies on their websites (see Table 5.6): the Washington VAAC studies can be found at *http://www.ssd.noaa.gov/PS/SAMPLES/* and the Darwin VAAC studies at *http://www.bom.gov.au/info/vaac/images.shtml*

Table 5.6. Locations of the nine Volcanic Ash Advisory Centers (VAACs), satellites used to generate ash products, and the principal dispersion model(s) utilized. The current URL is also given where available.

VAAC	*Region*		*Satellites*	*Dispersion model*
	Longitude (°E)	*Latitude* (°N)		
Anchorage[a]	(150, −135)	(50, 90)	GOES, POES, MODIS	Puff, HYSPLIT, CanERM
Buenos Aires[b]	(−90, −10)	(−90, −10)		
Darwin[c]	(75, 160)	(−90, 10)	MTSAT, POES, MODIS	HYSPLIT
London[d]	(−30, 60)	(45, 90)	MSG, MODIS, MetOp	NAME
Montreal[e]	(−135, 0)	(45, 90)	GOES-E, GOES-W	CanERM
Tokyo[f]	(90, 165)	(15, 60)	MTSAT, POES	Puff
Toulouse[g]	(−30, 90)	(−90, 70)	MSG, MetOp, MODIS	Media, MOCAGE
Washington[h]	(−150, −40)	(−10, 45)	GOES, POES, OMI	HYSPLIT
Wellington[i]	(160, −140)	(−90, 0)	MTSAT, POES	HYSPLIT

[a] *http://vaac.arh.noaa.gov/*
[b] *http://www.meteofa.mil.ar/vaac/vaac.htm*
[c] *http://www.bom.gov.au/info/vaac/*
[d] *http://www.metoffice.gov.uk/aviation/vaac/index.html*
[e] *http://meteo.gc.ca/eer/vaac/index_e.html*
[f] *http://ds.data.jma.go.jp/svd/vaac/data/index.html*
[g] *http://ds.data.jma.go.jp/svd/vaac/data/index.html*
[h] *http://www.ssd.noaa.gov/VAAC/washington.html*
[i] *http://vaac.metservice.com/vaac/*

Table 5.7. Summary of ash detection algorithms and techniques used with satellite infrared (IR) and visible channel data (RA = reverse absorption; TVAP = Three-channel volcanic ash product; PCI = principal component image; RAT = ratio method; WVC = water vapor correction method).

Name	*Principle*	*Reference*
RA	Two-band IR (11 and 12 μm)	Prata (1989a, b)
Ratio	Two-band IR (11 and 12 μm)	Holasek and Rose (1991)
Four-band	IR + visible	Mosher (2000)
TVAP	Three-band IR (3.9, 11, and 12 μm)	Ellrod *et al.* (2003)
PCI	Multi-band principal components	Hillger and Clark (2002a, b)
WVC	Two-band IR + water vapor correction	Yu *et al.* (2002)
RAT	Three-band IR (3.5, 11, and 12 μm)	Pergola *et al.* (2004)
Three-band	Three-band (IR and visible)	Pavolonis *et al.* (2006)

5.11.2 Ash measurements from geosynchronous platforms

Polar-orbiting instruments are much better suited for remote sensing at high latitudes, and some sophisticated systems have been developed utilizing AVHRR and MODIS data. For AVHRR and MODIS measurements it is possible to obtain up to six images per day from each satellite in the polar regions. With two satellites this gives hourly coverage compared with four times daily at low latitudes. Geosynchronous satellites, on the other hand, provide very high temporal frequency (15 min sampling in some cases) but, with a total field of view of 70° centered at the equator, coverage at high latitudes is limited. Nevertheless, geosynchronous sensors offer some interesting possibilities for ash cloud sensing at high latitudes by exploiting the oblique views offered. Gu *et al.* (2005) have shown that oblique viewing enhances the ash signal due to the longer path lengths obtained through the cloud. They demonstrated the effect for measurements of the 2001 Cleveland eruption and showed that enhancements of −8 K were evident compared with −3 K for measurements from MODIS. Prata and Barton (1994) showed through RT modeling that some quite complex behavior is possible for oblique viewing with the possibility of the reverse absorption effect disappearing (this will almost certainly occur as the opacity of the cloud gets larger) or even giving an opposite effect, similar to the arch shape observed for semi-transparent ice clouds. Another related aspect of using oblique viewing combined with high temporal resolution was demonstrated for the Kasatochi eruption that started on August 7, 2008. In this case, oblique viewing clearly showed the emergence of an erupting ash cloud through an extensive layer of meteorological cloud. This is shown in the panels of Figure 5.25, which are separated in time by 10–30 min. Cloud shadows thrown onto the meteorological deck of clouds below the emerging ash column can be used to calculate the height of the ash column. After 2 hours the ash cloud disperses in a southeasterly direction and becomes indistinguishable from meteorological clouds.

At low latitudes geosynchronous sensors have already proven to be extremely useful for monitoring ash clouds (e.g., Malingreau and Kaswanda, 1986; Sawada, 1987, 1996; Tupper *et al.*, 2004, 2007; Prata and Kerkmann, 2007), but their use at high latitudes has not been fully appreciated or exploited.

5.11.3 Examples of ash discrimination at high latitudes

The detection of ash clouds in the atmosphere using IR measurements is often confounded by the presence of water vapor, ice, and water clouds. There is a strong latitudinal dependence of water vapor in the atmosphere, with highest amounts near the equator and smallest amounts near the poles. From this we anticipate that, in general, it is easier to detect ash clouds in the polar (drier) regions. However, water vapor can be spatially and temporally quite variable and this is why robust ash detection

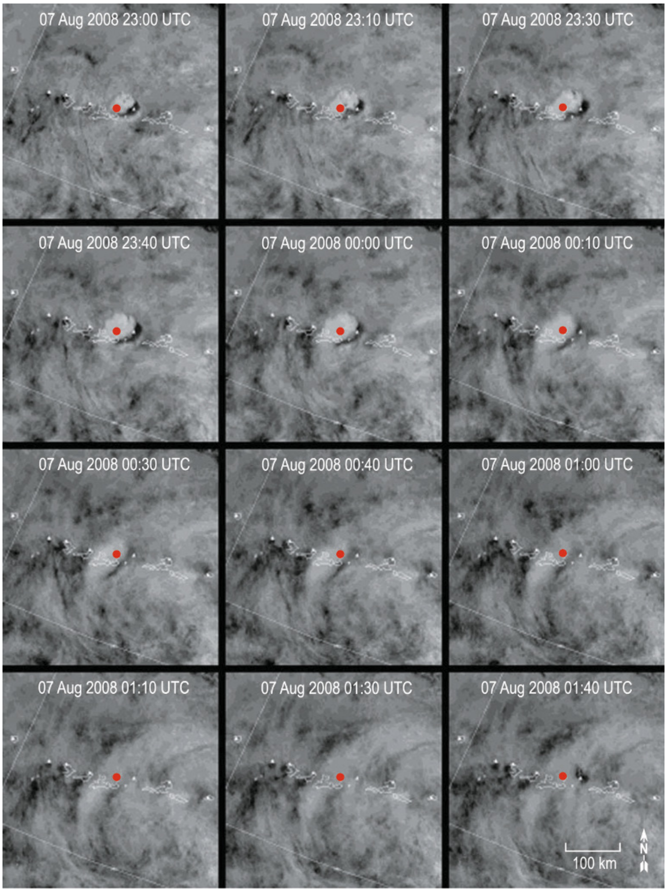

Figure 5.25. Sequence of GOES geosynchronous images of the eruption from Kasatochi Volcano, 2008. The oblique view of the sensor provides an excellent means for observing the ash column as it penetrates an existing cloud deck, and the subsequent dispersal of the ash cloud can be tracked using these high temporal resolution images. The red dot shows the location of the volcano.

schemes attempt to correct for water vapor (e.g., Gu *et al.*, 2003). Water and ice clouds are ubiquitous throughout the atmosphere but, within the moist tropics near strong convective regions, towering cumulonimbus clouds can form. These are ice rich with mixed-phase clouds and can spread over large areas. Persistent cloudiness is associated with mid-latitude baroclinic zones and frontal systems, and these can cause problems for ash detection, as was observed during the 2001 eruptions of Cleveland among others (Simpson *et al.*, 2002; Webley *et al.*, 2008). Cloudiness can also form around volcanoes generated by thermal heat or during the ascent of the eruption column through entrainment, nucleation, and cloud condensation. Although there do not appear to be any algorithms designed to operate in specific geographical regions,[3] it is useful to provide examples separately for high-latitude and low-latitude regions.

Holasek *et al.* (1996) described the use of satellite data for studying the eruptions of Augustine in 1986, a high-latitude volcanic eruption. For the example, we choose a more recent event, the eruption of Kasatochi in 2008, which also provides some

---

[3] The algorithms developed by Pergola *et al.* (2004) utilize climatological data and are geographically dependent, but have only been tested for the Mediterranean region around Sicily. Gu *et al.* (2005) have shown certain advantages when using GOES data at high latitudes for ash detection.

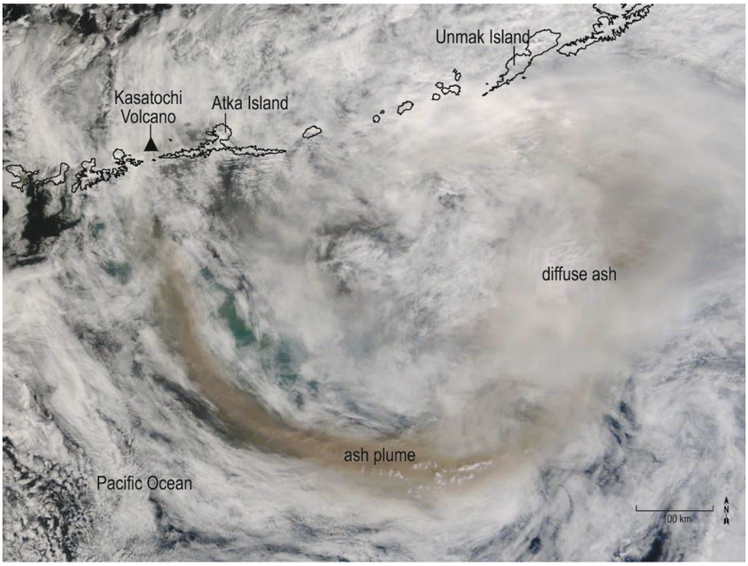

Figure 5.26. True-color MODIS image of the ash plume from Kasatochi Volcano on August 8, 2008.

salient features of ash detection. Kasatochi erupted on August 7, 2008 (*http://www.volcano.si.edu/world/volcano.cfm?vnum = 1101-13-&volpage = var#bgvn_3307*) sending ash and SO_2 up to 15 km and spreading ash some 1,200 km in a SE direction, while the SO_2 was dispersed across Canada, the continental U.S.A., and on to Europe and Russia. A true-color MODIS image of the ash plume on August 8 is shown in Figure 5.26. The ash is seen as a discolored filamental cloud overlying other meteorological clouds, displayed in shades of gray to white. Any ash below these meteorological clouds is not detectable using visible or infrared measurements. Some parts of the ash cloud are quite diffuse and can be discriminated from other clouds through context and continuity with thicker, brown-colored filaments. By using the ash retrieval scheme described earlier, the distribution of the mass of fine ash ($r < 10\,\mu m$) can be determined (Figure 5.27). The ash density has values as high as $10\,t\,km^{-2}$ ($10\,g\,m^{-2}$), and the total mass in the cloud is about 220 kt. A feature of this eruption was that it emitted a significant amount of SO_2, and this was tracked for much longer and over much greater distances than the ash.

There is a strong indication that the ash and SO_2 were collocated in the Kasatochi volcanic clouds, and this is demonstrated in Figure 5.27, where SO_2 column amounts (in DU) are plotted with the ash concentrations. The SO_2 columns were determined using AIRS $7.3\,\mu m$ measurements obtained at the same time but from a different instrument and a different spectral region and, so, may be considered as independent of the MODIS measurements. There is a clear indication that the SO_2 and ash are collocated and traveling together. Unfortunately, ash detection sensitivities are not as good as SO_2 sensitivities, so it is not possible to estimate for how long the ash persisted with the SO_2. In this instance there is a strong case to be made for using SO_2 measurements as a surrogate for ash, but this is by no means a universal assumption.

5.11.4 Examples of ash discrimination at low latitudes

For completeness we show how it is still possible, under favorable conditions, to determine geophysical parameters for ash clouds using infrared satellite data in the moist tropics. The eruption of Ruang, situated at the tip of Sulawesi in Indonesia, on September 25, 2002 was captured by several satellite sensors and has been discussed by Tupper *et al.* (2004) and Prata and Bernardo (2007). The initial eruption formed a tall, light-colored ash-rich column that rose over the Sangihie Islands (2.28°N, 125.43°E, 725 m) and, subsequently, dispersed west-

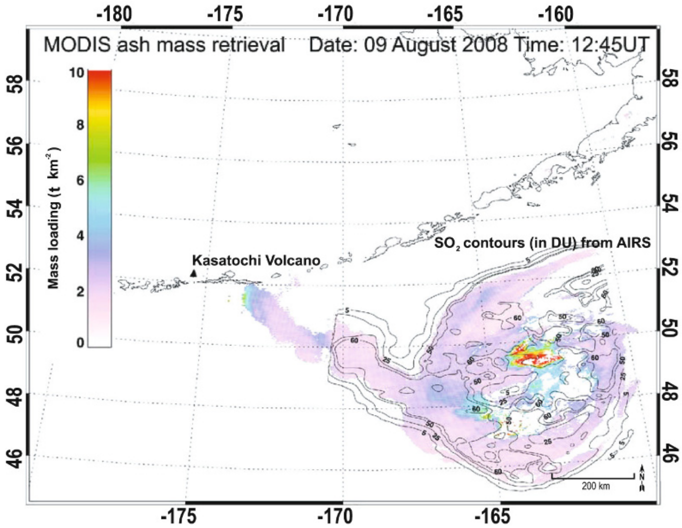

Figure 5.27. MODIS ash mass retrieval for an eruption from Kasatochi. Also shown are SO_2 contours (partial column in DU) derived from the AIRS sensor (see Prata and Bernardo, 2007).

wards, southwards, and eastwards (Figure 5.20a). It is likely that branches moving in different directions were at different heights and contained different volcanic material. The westward and southwestward-moving branches probably contained the majority of ash and some SO_2 and reached heights of up to 10–15 km. The faster moving eastward branch was at about 20 km and contained mostly SO_2. Unlike the previous example, this case shows that relying on SO_2 as a marker for ash would be unreliable, although it would still be advisable to avoid the SO_2 cloud, which may or may not have contained sufficient ash to be a hazard to aircraft. Figure 5.28 shows MODIS ash masses determined during the night-time overpass of the Aqua satellite, together with concurrent AIRS SO_2 retrievals. Note that AIRS suggests a significant SO_2 cloud traveling southwards, while the MODIS retrievals indicate little ash in this portion of the cloud, indicating that ash–gas separation has occurred (Holasek *et al.*, 1996).

5.11.5 Extensions

There are now several ash detection algorithms in use or proposed, based on IR and visible satellite data. Table 5.7 shows a summary of ash detection schemes (with original references), based mostly on using infrared channels. Several of these techniques show great promise for detecting volcanic ash, but there are important nuances and caveats associated with all of these techniques (including the two-channel, reverse absorption method) and we strongly recommend that the interested reader examine the original papers (listed in Table 5.7) carefully.

The two-channel, reverse absorption technique is very useful in cases where the ash is not too thick and not too dispersed; it is used at the VAACs (Watkin, 2003). The problems and pitfalls of using the reverse absorption technique have been discussed in the research literature (e.g., Simpson *et al.*, 2000; Prata *et al.*, 2001) and are well known to experienced meteorological analysts. Context is a key element in determining whether a particular cloud is an ash hazard or not, and trained meteorologists tasked with identifying ash clouds will use multiple sources of information including satellite imagery, pilot reports, ground observer reports, wind trajectories, and background information regarding regional volcanic activity and prior behavior.

Two of the instruments listed in Table 5.4 are capable of measuring much more than ash mass loadings. These instruments, AIRS and IASI, have high spectral resolution and, by utilizing more measurement channels, it may be possible to infer something about the mineralogy of the ash. Indeed, it may also be possible to discriminate dust (Figure 5.20g) and wind-blown ash (Figure 5.20h) out-

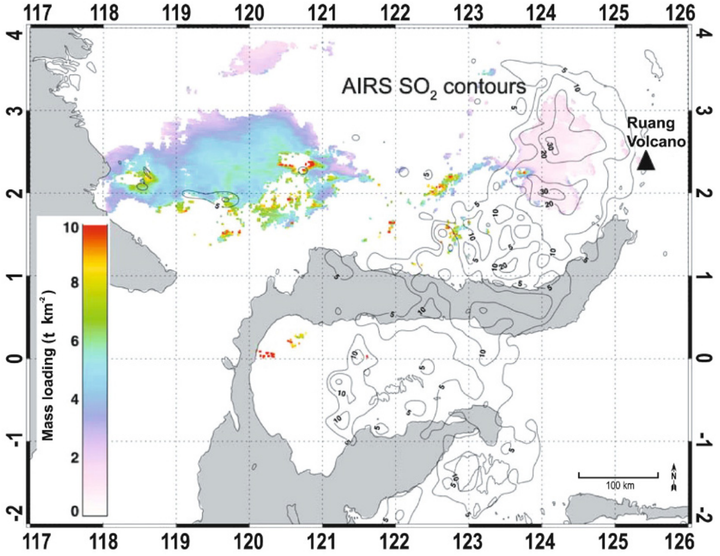

Figure 5.28. Ash mass concentrations in t km^{-2} (or g m^{-2}) for an eruption cloud from the eruption of Ruang, September 25, 2002. Also shown are contours of SO$_2$ amount (partial column in DU) derived from the AIRS spectrometer.

breaks from volcanic ash eruption clouds and plumes. Clerbaux *et al.* (2007) have shown the potential of IASI for measuring volcanic SO$_2$.

The analysis described above was predicated on the assumption that just a few (typically two) channels are available in the IR to discriminate ash from other airborne substances and perform retrievals. With AIRS and IASI, more than 2,000 channels are available, and this opens up possibilities for doing more elaborate retrievals and also providing more constraints of the retrieval which usually leads to more accurate solutions. The same theory may be used in the case of high spectral resolution IR data.

Figure 5.29 shows a spectral transect (all AIRS lines along a single AIRS column) as a function of wavenumber and contains a daunting amount of information. We may extend the ideas developed earlier to this high spectral domain in a simple manner. The reverse absorption or two-channel technique can be seen as a special case of sampling from a continuous spectral signature due to ash or water/ice clouds, now amenable to analysis from AIRS and IASI measurements. To illustrate how these signatures can be used in AIRS data, Figure 5.30 shows the ratio between the spectral brightness temperature (BT) and a reference brightness temperature at 1,000 cm^{-1} (BT$_{\text{ref}}$)[4] for six scene elements. The idea behind dividing by a reference brightness temperature is to approximate the emissivity variation of the spectra; the choice of 1,000 cm^{-1} is arbitrary, but it is necessary to avoid absorption regions and the region around 1,000 cm^{-1} is quite transparent. Within the region between 850 and 1,000 cm^{-1}, the ratio for ice (blue line) increases with wavenumber, whereas for ash and desert dust it decreases. For a clear atmosphere there is a slight increase with wavenumber due to water vapor absorption. Water clouds generally have a slope between that of the ice cloud and the clear scene. Ice and water clouds behave this way because the radiance spectra for ice and water over this region decrease with increasing wavenumber, which is a consequence of the decrease in cloud emissivity with increasing wavenumber, which in turn is related to the spectral variation of the refractive indices of ice and water. This change of slope of the spectral ratio with wavenumber can be used to discriminate ash from ice, water clouds, and clear scenes. The slopes are also sensitive to the optical depth of the cloud as well as the microphysics of the particles (refractive index, size, size distribution, and shape).

---

[4] The use of wavenumber ν (in cm^{-1}) instead of wavelength λ (in μm) is deliberate here because AIRS and IASI use this unit: $\nu(\text{cm}^{-1}) = 10{,}000/\lambda(\mu\text{m})$.

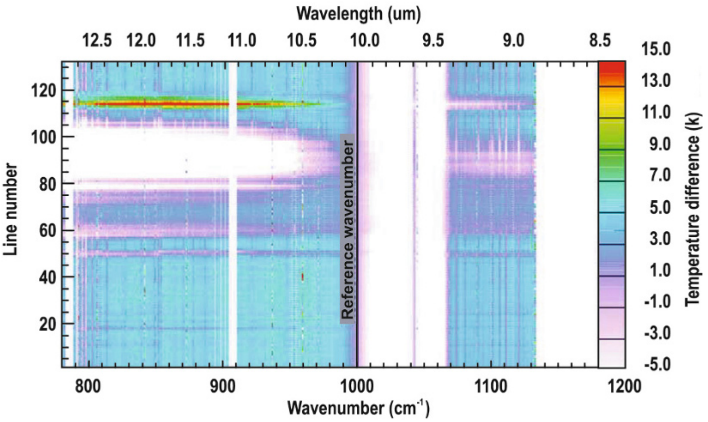

Figure 5.29. AIRS spectrum shown as a transect along a constant pixel number. The brightness temperature at 1,000 cm^{-1} has been subtracted from the spectra and plotted as brightness temperature differences (BTDs).

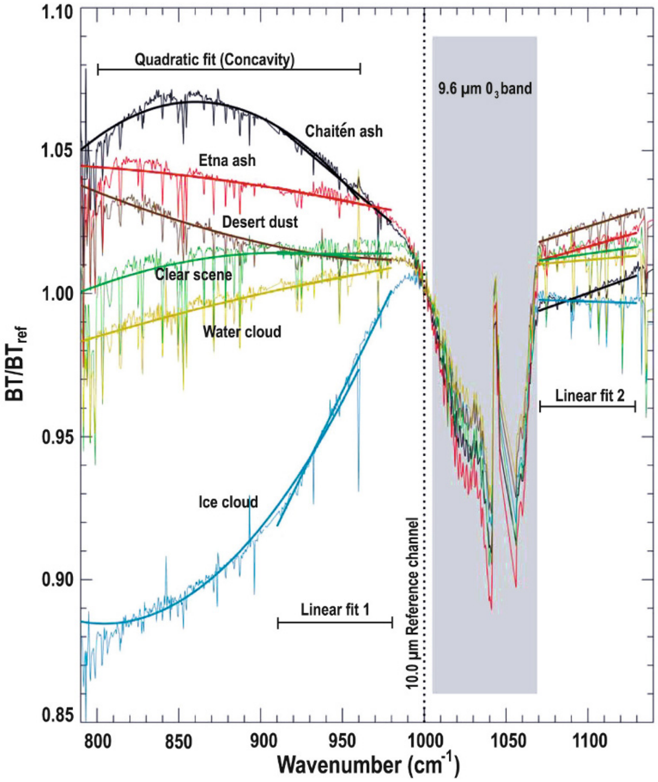

Figure 5.30. Spectral ratio of the top-of-atmosphere brightness temperature for a single AIRS pixel and for six different scenes: (1) a pixel containing a semi-transparent ice cloud (blue line), (2) a water cloud (yellow line), (3) a clear pixel (green line), (4) desert dust (brown line), (5) a pixel affected by ash from an eruption of Etna (red line), and (6) a Chaitén ash-affected pixel (black line). The grayed-out region includes the strong O_3 absorption and is not used in the analyses. The spectral regions where linear and quadratic fits are performed are also indicated on the plot.

Spectral fits (rather than channel differences) can be performed to obtain objective parameters for discriminating ash, water, ice, and other airborne substances. These fits are shown in Figure 5.30, labeled as "the concavity" (a quadratic fit) and two linear fits. Furthermore, the shape or signature of the spectral variation is sensitive to many parameters, including particle size and composition. By using a detailed RT model it may be possible to infer, for the first time, the composition of ash in the atmosphere providing useful insights into processes occurring in the interior of a volcano.

5.12 DIFFICULTIES AND FUTURE RESEARCH

Perhaps the greatest hindrance to detection and discrimination of volcanic ash clouds arises from interference effects from liquid water droplets and ice particles. Simpson *et al.* (2001) drew attention to the issue of water vapor absorption effects on the reverse absorption algorithm, but the analyses in that paper contained numerous errors and lacked rigor (Prata *et al.*, 2001). Many of the problems with ash detection have been described in the literature (Prata, 1989a, b; Rose *et al.*, 1995; Schneider *et al.*, 1995, 1999; Prata and Grant, 2001; Prata *et al.*, 2001; Dean *et al.*, 2002, 2004; Webley *et al.*, 2008) and at various workshops, symposia, and conferences. A further issue, still not fully resolved and of some importance, is the difficulties surrounding separation of ash and SO_2 in dispersing volcanic clouds. It had been thought that there is often significant (detectable) SO_2 emitted with ash during an explosive eruption. The eruption of Chaitén Volcano in southern Chile (Carn *et al.*, 2009) showed the opposite, as large amounts of ash were transported over significant distances with just minor SO_2 emissions. These observations reinforce the need to have robust ash detection algorithms together with SO_2 algorithms and indicate that research into improved ash retrieval schemes using a variety of satellite tools is warranted.

It seems possible, with sufficient spectral information, to isolate the main effects due to the various airborne volcanic substances. If ash particles are encased by ice then the characteristic infrared signature cannot be detected and some other means of detection is warranted. Rose *et al.* (2004) have elucidated the times and places when ice is likely to be present in volcanic clouds. Combinations of sensors and techniques will be required if further advances are to be made in volcanic ash detection. The recent use of active methodologies (e.g., ground-based radar and the space-borne lidar Caliop; Winker *et al.*, 2007) provides new insights into the properties of volcanic clouds. Active sensors also provide range information, sadly lacking from the current operational suite of instruments. The way forward will utilize a multitude of sensors (passive and active), wavelengths (ultraviolet, visible, infrared, and microwave; Constantine *et al.*, 2000), and platforms (e.g., satellite and ground-based) and combine these measurements with dispersion models, models of ash column generation (e.g., ATHAM; Oberhuber *et al.*, 1998), and knowledge gained from geophysical data derived from seismic and other more traditional volcanological tools. Recent work by Pavolonis (2010) has extended the reverse absorption method demonstrating a robust scheme that gives fewer false alarms and that has the potential to be fully automated. The scheme can be used with any of the satellite sensors with the appropriate infrared bands and utilities independent of meteorological data. The scheme also includes a method for estimating cloud top height.

5.13 REFERENCES

Bailey, J.E.; Dean, K.; Dehn, J.; Webley, P. (2010). Integrated satellite observations of the 2006 eruption of Augustine Volcano, in J.A. Power, M.L. Coombs, and J.T. Freymueller (Eds.), *The 2006 Eruption of Augustine Volcano, Alaska* (USGS Professional Paper 1769), U.S. Geological Survey, Reston, VA, pp. 481–506.

Barton, I.J.; Prata, A.J.; Watterson, I.G.; Young, S.A. (1992). Identification of the Mount Hudson volcanic cloud over SE Australia, *Geophys. Res. Lett.*, **19**, 1211–1214.

Berk, A.; Bernstein, L.S.; Robertson, D.C. (1989). *MODTRAN: A Moderate Resolution Model for LOWTRAN 7* (AFGL-TR-89-0122), U.S. Air Force Phillips Laboratory, Nascom Air Force Base, MA.

Bluth, G.J.S.; Doiron, S.D.; Krueger, A.J.; Walter, L.S.; Schnetzler C.C. (1992). Global tracking of the SO_2 clouds from the June, 1991 Mount Pinatubo eruptions, *Geophys. Res. Lett.*, **19**, 151–154.

Briggs, G.A. (1975). Plume rise predictions, in *Lectures on Air Pollution and Environmental Impact Analyses*, American Meteorological Society, Boston, pp. 59–111.

Carn, S.A.; Pallister, J.S.; Lara, L.; Ewert, J.W.; Watt, S.; Prata, A.J., Thomas, R.J.; Villarosa, G. (2009). The unexpected awakening of Chaitén Volcano, Chile, *EOS Trans.*, **90**(24), 205–206.

Casadevall, T.J. (1994). The 1989/1990 eruption of Redoubt Volcano Alaska: Impacts on aircraft operations, *J. Volcanol. Geothermal Res.*, **62**(30), 301–316.

Casadevall, T.J.; Delos Reyes, P.J.; Schneider, D.J. (1996). The 1991 Pinatubo eruptions and their effects on aircraft operations, in C.G. Newhall and R.S. Punongbayan (Eds.), *Fire and Mud: Eruptions and Lahars of Mount Pinatubo, Philippines*, Philippines Institute of Volcanology and Seismology/University of Washington Press, Quezon City/Seattle, WA, pp. 625–636.

Clerbaux, C.; Turquety, S.; Hadji-Lazaro, J.; George, M.; Boynard, A.; Pommier, M.; Coheur, P.-F.; Hurtmans, D.; Wespes, C.; Razavi, A. (2007). Monitoring of volcanic SO_2 using thermal infrared IASI/METOP sounders (TES, IASI), paper presented at the *Support to Aviation Control Service Meeting, Toulouse, France, November 26–27, 2007*.

Constantine, E.K.; Bluth, G.J.S.; Rose, W.I. (2000). TOMS and AVHRR sensors applied to drifting volcanic clouds from the August 1991 eruptions of Cerro Hudson, in P. Mouginis-Mark, J. Crisp, and J. Fink (Eds.), *Remote Sensing of Active Volcanism* (AGU Monograph 116), American Geophysical Union, Washington, D.C., pp. 45–64.

Dean, K.; Bowling, S.A.; Shaw, G.; Tanaka, H. (1994). Satellite analyses of movement and characteristics of the Redoubt volcano plume, January 8, 1990, *J. Volcanol. Geothermal Res.*, **62**, 339–352.

Dean, K.; Dehn, J.; Engle, K.; Izbekov, P.; Papp, K.; Patrick, M. (2002). Operational satellite monitoring of volcanoes at the Alaska Volcano Observatory, *Adv. Environ. Monit. Model.*, **1**, 3–35.

Dean, K.G.; Dehn, J.; Papp, K.R.; Smith, S.; Izbekov, P.; Peterson, R.; Kearney, C.; Steffke, A. (2004). Integrated satellite observations of the 2001 eruption of Mt. Cleveland, Alaska, *J. Volcanol. Geothermal Res.*, **135**, 51–73.

Ellrod, G.P.; Connell, B.H.; Hillger, D.W. (2003). Improved detection of airborne volcanic ash using multispectral infrared satellite data, *J. Geophys. Res.*, **108**(D12), 4356, doi: 10.1029/2002JD002802.

Evans, B.T.N. (1988). *An Interactive Program for Estimating Extinction and Scattering Properties of Moist Particulate Clouds* (Department of Defence Report MRL-R-1123), Defence Science & Technology Organisation, Materials Research Laboratory, Ascot Vale, Victoria, Australia.

Fierstein, J. (2007). Explosive eruptive record in the Katmai region, Alaska Peninsula: An overview, *Bull. Volcanol.*, **69**, 469–509.

Glenkova, I.; Seiz, G.; Zuidema, P.; Zhao, G.; Di Girolamo, L. (2007). Cloud top height comparisons from ASTER, MISR and MODIS for trade wind cumuli, *Rem. Sensing Env.*, **107**, 211–222.

Gu, Y.; Rose, W.I.; Bluth, G.J.S. (2003). Retrieval of mass and sizes of particles in sandstorms using two MODIS IR bands: A case study of April 7 2001 sandstorm in China, *Geophys. Res. Lett.*, **30**(15), 1805, doi: 10.1029/2003GL017405.

Gu, Y.; Rose, W.I.; Schneider, D.J.; Bluth, G.J.S.; and Watson, I.M. (2005). Advantageous GOES IR results for ash mapping at high latitudes: Cleveland eruptions 2001, *Geophys. Res. Lett.*, **32**, L02305, doi: 10.1029/2004GL021651.

Hanstrum, B.N.; Watson, A.S. (1983). A case study of two eruptions of Mount Galunggung and an investigation of volcanic eruption cloud characteristics using remote sensing techniques, *Aust. Met. Mag.*, **31**, 131–177.

Harris, D.M.; Rose, W. (1983). Estimating particle sizes, concentration, and total mass of volcanic ash clouds using weather radar, *J. Geophys. Res.*, **88**, 10969–10983.

Harris, D.M.; Rose, W.; Roe, R.; Thompson, M.R. (1981). Radar observations of ash eruptions, in P.W. Lipman and D.R. Mullineaux (Eds.), *The 1980 Eruptions of Mount St. Helens, Washington* (USGS Circular 1250), U.S. Geological Survey, Reston, VA, pp. 323–333.

Hasler, A.F. (1981). Stereographic observations from geosynchronous satellites: An important new tool for the atmospheric sciences, *Bull. Amer. Meteorol. Soc.*, **62**(2), 194–212.

Hillger, D.W.; Clark, J.D. (2002a). Principal component image analysis of MODIS for volcanic ash, Part I: Most important bands and implications for future GOES imagers, *J. Appl. Meteorol.*, **41**, 985–1001.

Hillger, D.W.; Clark, J.D. (2002b). Principal component image analysis of MODIS for volcanic ash, Part II: Simulation of current GOES and GOES-M imagers, *J. Appl. Meteorol.*, **41**, 1003–1010.

Hofmann, D.J.; Rosen, J.M. (1984). On the temporal variation of stratospheric aerosol size and mass during the first 18 months following the 1982 eruptions of El Chichón, *J. Geophys. Res.*, **89**(D3), 4883–4890, doi: 10.1029/JD089iD03p048833.

Holasek, R.E.; Rose, W.I. (1991). Anatomy of 1986 Augustine Volcano eruptions as recorded by multispectral image processing of digital AVHRR weather satellite data, *Bull. Volcanol.*, **53**, 420–435.

Holasek, R.; Self, S. (1995). GOES weather satellite observations and measurements of the May 18, 1980, Mt. St. Helens eruption, *J. Geophys. Res.*, **100**, 8469–8487.

Holasek, R.E.; Woods, A.W.; Self, S. (1996). Experiments on gas–ash separation processes in volcanic umbrella clouds, *J. Volcanol. Geothermal Res.*, **70**, 169–181.

Holton, J. (2004). *An introduction to Dynamic Meteorology*, Academic Press, San Diego, CA, pp. 116–117 .

Ivlev, L.S.; Popova, S.I. (1973). The complex refractive indices of substances in the atmospheric aerosol dispersed phase, *Atmospheric Oceanic Physics*, **9**(10), 587–591.

Kearney, C. (2010). The effects of silicate ash on thermal infrared sulfur dioxide retrievals, Unpublished doctoral dissertation, University of Bristol, Bristol, U.K.

Kennedy, B.; Spieler, O.; Scheu, B.; Kueppers, U.; Taddeucci, J.; Dingwell, D.B. (2005). Conduit implosion during Vulcanian eruptions, *Geology*, **33**, 581–584, doi: 10.1130/G21488.1.

King, M.D., Harshvardhan; Arking, A. (1984). A model of the radiative properties of the El Chichón stratospheric layer, *J. Climate Appl. Meteorol.*, **23**, 1121–1137.

Lacasse, C.; Karlsdóttir, S.; Larsen, G.; Soosalu, H.; Rose, W.I.; Ernst, G.G.J. (2004). Weather radar observations of the Hekla 2000 eruption cloud, Iceland. *Bull. Volcanol.*, **66**, 457–473.

Lane, S.J.; Gilbert, J.S.; Kemp, A.J. (1995). Electrical and chemical properties of eruption plumes at Sakurajima volcano, Japan. In: *Eighth Report of Geophysical and Geochemical Observations at Sakurajima Volcano*, Sakurajima Volcano Research Center, Sakurajima, Japan, pp. 105–127.

Lutgens, F.K.; Tarbuck, E.J. (1986). *The Atmosphere: An Introduction to Meteorology*, Prentice-Hall, Englewood Cliffs, NJ, pp. 154–160.

Lutgens, F.K.; Tarbuck, E.J. (1995). *The Atmosphere*, Prentice-Hall, Englewood Cliffs, NJ, 462 pp.

Lynch, J.S.; Stephens, G. (1996). Mount Pinatubo: A satellite perspective of the June 1991 eruptions, in C. Newhall and R.S. Punongbayan (Eds.), *Fire and Mud*, University of Washington Press, Seattle, WA, pp. 637–646.

Malingreau, J.-P.; Kaswanda (1986). Monitoring volcanic eruptions in Indonesia using weather satellite data: The Colo eruption of July 28, 1983, *J. Volcanol. Geothermal Res.*, **27**(1/2), 179–194.

Manins, P.C. (1985). Cloud heights and stratospheric injections resulting from a thermonuclear war, *Atmos. Environ.*, **19**(8), 1245–1255.

Marzano, F.S.; Vulpiani, G.; Rose,W.I. (2006). Microphysical characterization of microwave radar reflectivity due to volcanic ash clouds, *IEEE Trans. Geosci. Remote Sens.*, **44**, 313–327.

Masuda, K.; Takashima, T. (1990). Deriving cirrus information using the visible and near-ir channels of the future NOAA-AVHRR radiometer, *Remote Sens. Environ.*, **31**, 65–81.

Matson, M. (1984). The 1982 El Chichón volcano eruptions: A satellite perspective, *J. Volcanol. Geothermal Res.*, **23**, 1–10.

Miller, T.P.; Casadevall, T.J. (1999). Volcanic ash hazards to aviation, in H. Sigurdsson, B. Houghton, S.R. McNutt, H. Ryman, and J. Stix (Eds.), *Encyclopedia of Volcanoes*, Academic Press, San Diego, CA, pp. 915–930.

Miller, T.P., Chouet, B.A. (1994). The 1989–1990 eruptions of Redoubt Volcano: An introduction, *J. Volcanol. Geothermal Res.*, **62**, 1–10, doi: 10.1016/0377-0273(94)90025-6.

Mosher, F.R. (2000). Four channel volcanic ash detection algorithm, *Preprint Volume: 10th Conference on Satellite Meteorology and Oceanography, January 9–14, 2000, Long Beach, California*, pp. 457–460.

Newell, R.E.; Deepak, A. (Eds.) (1982). *Mount St. Helens Eruptions of 1980: Atmospheric Effects and Potential Climate Impact* (NASA Workshop Report, NASA SP-458), Scientific and Technical Information Branch, NASA,Washington, D.C., 119 pp.

Oberhuber, J.M.; Herzog, M.; Graf, H.; Schwanke, K. (1998). Volcanic plume simulation on large scales, *J. Volcanol. Geothermal Res.*, **87**(1/4), 29–53.

Oswalt, J.S.; Nichols, W.; O'Hara, J.F. (1996). Metereological observations of the 1991 Mount Pinatubo eruption, in C. Newhall and R.S. Punongbayan (Eds.), *Fire and Mud: Eruption and Lahars of Mount Pinatubo, Philippines*, University of Washington Press, Seattle, WA, pp. 625–636.

Pavolonis, M.J. (2010). Advances in extracting cloud composition information from spaceborne infrared radiances: A robust alternative to brightness temperatures, Part I: Theory, *J. Applied Meteorology and Climatology*, **49**, 1992–2012.

Pavolonis, M.J.; Feltz, W.F.; Heidinger, A.K.;d Gallina, G.M. (2006). A daytime complement to the reverse absorption technique for improved automated detection of volcanic ash, *J. Atmos. Oceanic Technol.*, **23**, 1422–1444.

Pergola, N.; Tramutoli, V.; Marchese, F.; Scaffidi, I.; Lacav, T. (2004). Improving volcanic ash cloud detection by a robust satellite technique, *Remote Sens. Environ.*, **90**, 1–22.

Pollack, J.B.; Toon, O.B.; Khare, B.K. (1973). Optical properties of some terrestrial rocks and glasses, *Icarus*, **19**, 372–389.

Prata, A. J. (1989a). Observations of volcanic ash clouds using AVHRR-2 radiances, *Int. J. Remote Sensing*, **10**(4/5), 751–761.

Prata., A.J. (1989b). Radiative transfer calculations for volcanic ash clouds, *Geophys. Res. Lett.*, **16**(11), 1293–1296.

Prata, A.J.; Barton, I.J. (1994). Detection and discrimination of volcanic ash clouds by infrared radiometry, I: theory, in T.J. Casadevall (Ed.), *Volcanic Ash and Aviation Safety: Proceedings of the First International Symposium on Volcanic Ash and Aviation Safety, Seattle, WA* (USGS Bulletin 2047), U.S. Geological Survey, Reston, VA, pp. 305–311.

Prata, A.J.; Bernardo, C. (2007). Retrieval of volcanic SO_2 column abundance from Atmospheric Infrared

Sounder data, *J. Geophys. Res.*, **112**, D20204, doi: 10.1029/2006JD007955.

Prata, A.J.; Grant, I.F. (2001). Retrieval of microphysical and morphological properties of volcanic ash plumes from satellite data: Application to Mt. Ruapehu, New Zealand., *Quart. J. Roy. Meteorol. Soc.*, **127**(576B), 2153–2179.

Prata, A.J.; Kerkmann, J. (2007). Simultaneous retrieval of volcanic ash and SO_2 using MSG-SEVIRI measurements, *Geophys. Res. Lett.*, **34**, L05813, doi: 10.1029/2006GL028691.

Prata, A.J.; Turner, P.J. (1997). Cloud-top height determination using ATSR data, *Remote Sens. Environ.*, **59**(1), 1–13.

Prata, A.J.; Bluth, G.J.S.; Rose, W.I.; Schneider, D.J.; Tupper, A.C. (2001). Comments on failures in detecting volcanic ash from a satellite-based technique. *Remote Sens. Environ.*, **78**, 341–346.

Press, W.H.; Flannery, B.P.; Teukolsky, S.A.; Vetterling, W.T. (1986). *Numerical Recipes*, Cambridge University Press, Cambridge, U.K., 818 pp.

Przedpelski, Z.J.; Casadevall, T.J. (1994). Impact of volcanic ash from 15 December 1989 Redoubt volcano eruption on GE CF6-80C2 turbofan engines, in *Volcanic Ash and Aviation Safety: Proceedings of the First International Symposium on Volcanic Ash and Aviation Safety, Seattle, WA, July 1991* (USGS Bulletin 2047), U.S. Geological Survey, Reston, VA, pp. 129–135,

Pyle, D.M. (1989). The thickness, volume and grainsize of tephra fall deposits. *Bull. Volcanol.*, **51**(1), 1–15.

Rose, W.I.; Kostinski, A.B.; Kelly, L. (1995a). *Real-Time C-Band Radar Observations of 1992 Eruption Clouds from Crater Peak, Mount Spurr Volcano, Alaska* (USGS Bull. 2139), U.S. Geological Survey, Reston, VA, pp. 19–26.

Rose, W.I.; Delene, D.J.; Schneider, D.J.; Bluth, G.J.S.; Kruger, A.J.; Sprod, I.; McKee, C.; Davies, H.L.; and Ernst, G.J. (1995b). Ice in the 1994 Rabaul eruption: Implications for volcanic hazard and atmospheric effects, *Nature*, **375**, 477–479.

Rose, W.I.; Bluth, G.J.S.; Ernst, G.G.J. (2000). Integrating retrievals of volcanic cloud characteristics from satellite remote sensors: A summary, *Phil. Trans. Roy. Soc. Lond., Ser. A: Mathematical, Physical, and Engineering Sciences*, **358**(1770), 1585–1606, doi: 10.1098/rsta.2000.0605.

Rose, W.I.; Bluth, G.J.S.; Watson I.M. (2004). Ice in volcanic clouds: When and where? *Proceedings of the Second International Conference on Volcanic Ash and Aviation Safety*, Office of the Federal Coordinator for Meteorological Services and Supporting Research, Washington, D.C., Session 3, p. 61.

Sawada, Y. (1987). *Study on Analysis of Volcanic Eruptions Based on Eruption Cloud Image Data Obtained by the Geostationary Meteorological Satellite (GMS)* (Technical Report 22), Meteorological Research Institute, Tsukuba, Japan, 335 pp.

Sawada, Y. (1996). Detection of explosive eruptions and regional tracking of volcanic ash clouds with geostationary meteorological satellites (GMS), in R. Scarpa and R.I. Tilling (Eds.), *Monitoring and Mitigation of Volcano Hazards*, Springer-Verlag, Berlin, pp. 299–314.

Schneider, D.J.; Rose, W.I.; Kelley, L. (1995). *Tracking of 1992 Eruption Clouds from Crater Peak of Mount Spurr Volcano, Alaska, Using AVHRR* (USGS Bulletin 2139), U.S. Geological Survey, Reston, VA, pp. 27–36.

Schneider, D.J.; Rose, W.I.; Coke, L.R.; Bluth, G.J.S. (1999). Early evolution of a stratospheric volcanic eruption cloud as observed with TOMS and AVHRR, *J. Geophys. Res.*, **104**(D4), 4037– 4050.

Scollo, S.; Folch, A.; Coltelli, M.; Realmuto, V.J. (2010). Three-dimensional volcanic aerosol dispersal: A comparison between Multiangle Imaging Spectro-Radiometer (MISR) data and numerical simulations, *J. Geophys. Res.*, **115**, D24210, doi: 10.1029/2009JD013162.

Searcy, C.; Dean, K.; Stringer, W. (1998). PUFF: A high-resolution volcanic ash tracking model, *J. Volcanol. Geothermal Res.*, **80**, 1–16.

Simpson, J.J.; Hufford, G.; Pieri, D.; Berg, J. (2000). Failures in detecting volcanic ash from a satellite-based technique, *Remote Sens. Environ.*, **72**, 191–217.

Simpson, J.J.; Berg, J.S.;Koblinsky, C.J.; Hufford, G.L.; Beckley, B. (2001). The NVAP Global Water Vapor Data Set: Independent cross-comparison and multi-year variability, *Remote Sensing of Environment*, **76**(1), 112–129, doi: 10.1016/S0034-4257(00)00199-1.

Simpson, J.J.; Hufford, G.; Pieri, D.; Servranckx, R.; Berg, J. (2002). The February 2001 Eruption of Mount Cleveland, Alaska: Case study of an aviation hazard, *Weather and Forecasting*, **17**, 691–704.

Sokolik, I.N.; Toon, O.B. (1999). Incorporation of mineralogical composition into models of the radiative properties of mineral aerosol from UV to IR wavelengths, *J. Geophys. Res.*, **104**(D8), 9423–9444.

Sparks, R.S.J.; Bursik, M.I.; Carey, S.N.; Gilbert, R.S.; Glaze, L.S.; Sigurdsson, H.; Woods, A.W. (1997). *Volcanic Plumes*, John Wiley & Sons, New York, 574 pp.

Stamnes, K.; Swanson, R.A. (1981). A new look at the discrete ordinates method for radiative transfer calculations in anisotropically scattering atmospheres, *J. Atmos. Sci.*, **38**, 387–399.

Stohl, A.; Prata, A.J.; Eckhardt, S.; Clarisse, L.; Durant, A.; Henne, S.; Kristiansen, N.I.; Minikin, A.; Schumann, U.; Seibert, P. *et al.* (2011). Determination of time- and height-resolved volcanic ash emissions for quantitative ash dispersion modeling: The

2010 Eyjafjallajökull eruption, *Atmos. Chem. Phys. Discuss.*, **11**, 5541–5588.

Tupper, A.; Oswalt, J.S. (2005). Satellite and radar analysis of the volcanic cumulonimbi at Mount Pinatubo, Philippines, 1991, *J. Geophys. Res.*, **110**(D09204), 1–15.

Tupper, A.; Kinoshita, K.; Kanagaki, C. (2003). Observations of volcanic cloud heights and ash–atmosphere interactions, *WMO/ICAO Third Workshop on Volcanic Ash, Toulouse, France, September 29–October 3*.

Tupper, A.; Carn, S.A.; Davey, J.; Kamada, Y.; Potts, R.J.; Prata, A.J.; Tokuno, M. (2004). An evaluation of volcanic cloud detection techniques during recent significant eruptions in the western Ring of Fire, *Remote Sens. Environ.*, **91**, 27–46.

Tupper, A.; Itikarai, I.; Richards, M.; Prata, F.; Carn, S.; Rosenfeld, D. (2007). Facing the challenges of the International Airways Volcano Watch: The 2004/05 eruptions of Manam, Papua New Guinea, *Weather and Forecasting*, **22**(1), 175–191.

Turco, R.P., Toon, O.B., Whitten, R.C., Hamill, P., and Keesee, R.G. (1983). The 1980 eruptions of Mt. St. Helens: Physical and chemical processes in the stratospheric clouds, *J. Geophys. Res.*, **88**, 5299–5319.

Turco, R.P. (1992). Physical and chemical processes of volcanic interactions with the atmosphere, in L.T. Simarski (Ed.), *Volcanism and Climate Change* (AGU Special Report), American Geophysical Union, Washington, D.C., p. 5.

Volz, F.E. (1973). Infrared optical constants of ammonium sulfate, Sahara dust, volcanic pumice, and fly ash, *Appl. Opt.*, **12**(3), 564–568.

Walker, G.P.L. (1971). Grain-size characteristics of pyroclastic deposits, *J. Geology*, **79**, 696–714.

Watkin, S.C. (2003). The application of AVHRR data for the detection of volcanic ash in a Volcanic Ash Advisory Center, *Meteorol. Appl.*, **10**, 301–311.

Watson, I.M.; Realmuto, V.J.; Rose, W.I.; Prata, A.J.; Bluth, G.J.S.; Gu, Y.; Bader, C.E.; Yu, T. (2004). Thermal infrared remote sensing of volcanic emissions using the moderate resolution imaging spectroradiometer, *J. Volcanol. Geothermal Res.*, **135**, 75–89.

Webley, P.W.; Atkinson, D.; Collins, R.L.; Dean, K.; Fochesatto, J.; Sassen, K.; Cahill, C.F.; Prata, A.J.; Flynn, C.J.; Mizutani, K. (2008). Predicting and validating the tracking of a volcanic ash cloud during the 2006 eruption of Mt. Augustine volcano, *Bull. Amer. Meteorol. Soc.*, 1647–1657, doi: 10.1175/2008BAMS2579.1, .

Wen, S.; Rose, W.I. (1994). Retrieval of sizes and total masses of particles in volcanic clouds using AVHRR bands 4 and 5, *J. Geophys. Res.*, **99**(D3), 5421–5431.

Winker, D.M.; Hunt, W.H.; McGill, M.J. (2007). Initial performance assessment of CALIOP, *Geophys. Res. Lett.*, **34**, L19803, doi: 10.1029/2007GL030135.

Wood, J.; Scott, C.; Schneider, D. (2007). WSR-88D radar observations of volcanic ash, *Fourth International Workshop on Volcanic Ash*, World Meterological Organization (WMO) in close collaboration with the International Civil Aviation Organziation (ICAO) and the Civil Aviation Authority of New Zealand, Rotorua, New Zealand.

Woods, A.W.; Self, S. (1992). Thermal disequilibrium at the top of volcanic clouds and its effect on estimates of the column height, *Nature*, **355**, 628–630.

Wylie, D.P.; Santek, D.; O'Starr, D. (1998). Cloud-top heights from GOES-8 and GOES-9 stereoscopic imagery, *J. Appl. Meteorol.*, **37**, 405–413.

Yu, T.; Rose, W.I.; Prata, A.J. (2002). Atmospheric correction for satellite-based volcanic ash mapping and retrievals using split window IR data from GOES and AVHRR, *J. Geophys. Res.*, **107**(D16), 4311, doi: 10.1029/2001JD000706.

Zobin, V.M.; Jiménez, M. (2008). Some regularity in the process of re-awakening of andesite and dacite volcanoes: Specific features of the 1982 El Chichón volcano, México reactivation, *J. Volcanol. Geothermal Res.*, **175**(4), 482–487